Microstructural Imaging of the Eye and Mechanical Mapping of Retinal Tissue using Atomic Force Microscopy (AFM)

by

©Asia Ahmed Alhasawi

A thesis submitted to the School of Graduate Studies in partial fulfillment of the requirements for the degree of

Master of Science

Department of Chemistry

Memorial University of Newfoundland

June 2016

St. John's Newfoundland

Abstract

The objective of this study is to investigate the structures and mechanical properties of mouse eyes in correspondence with their functions. Moreover, my work places particular emphasis on the retina as it is associated with several diseases. To measure the mechanical properties of retinal tissue, eye samples of mice are taken and analyzed utilizing Force Spectroscopy to determine the Young's modulus. Force mapping of the sample is done by nanoindentation (force curves), and Atomic Force Microscopy (AFM) is used to image the topography of our sample. AFM and force mapping provide key information on the nanoscale mechanical properties and structure of normal tissue. This fine level of detail provides insight on a length scale relevant to an individual cell.

Our results also provide a baseline structure to enable the identification of mechanical indicators for disease. Most of the diseases that affect the eyes, including glaucoma and macular degenerations involve structural changes in the eyes, for example, affecting the photoreceptor or degeneration of layers thus causing eye damage. Damage on the nanoscale is not obvious given that research in that area is still underdeveloped. Therefore, the use of nanomechanical mapping has proved to be very useful because of providing in-depth knowledge regarding the characteristic microstructure and mechanical features of the normal eye.

Acknowledgements

First of all, I would like to thank my supervisor Dr. Erika Merschrod for all her generosity and continued advice that she gave me since I started my masters degree until I finished it. It is my pleasure to be one of her students. I also would like to thank my committee members Dr. Peter Warburton and Dr. Bob Davis for all their time, advice, and comments.

I am thankful to all Merschrod's group, and give special thanks to the bio members: Lucas D. Stewart, Zhe Dong, David James Gale, Garrett McDougall, and Ryan Wilkins. Also, I am thankful to Dr. Robert Gendron, who provided us with eye samples, for all his guidance and support that was needed.

A huge thanks to my family, my husband (Mohammed Alhasawi), and my kids: Ali, Fatimah, and Albatol for all the support during my studies. I really couldn't make it without their help and support. I am grateful to my mom, dad, sisters and brothers who encouraged me to complete my degree after facing lots of challenge finding acceptance in Canada.

I am also thankful to the department of Chemistry and School of Graduate Studies. Last but not least, I would like to thank the Saudi Cultural Bureau in Canada for their funding during my studies. This research was also supported in part by funding from NSERC and CFI.

Table of Contents

List of Tables

List of Figures

List of Abbreviations and Symbols

Å	Ångstrom
AFM	atomic force microscopy
AMD	age-related macular degeneration
ANOVA	analysis of variance
DF	degrees of freedom
DFL	deflection signal
DLVO	Derjaguin-Landau-Verwey-Overbeek
DMT	Derjaguin-Muller-Toporov
E	Young's modulus
F	F-test value (ratio of variances)
Fc	critical F-test value
Fp	Welch statistic
Fpc	critical value for Fp
invOLS	inverse optical lever sensitivity
JKR	Johnson-Kendall-Roberts
LC	lamina cribros
MD	macular degeneration
MS	mean square
P	calculated probability

PE	pigment epithelium
pLC	post-laminar cells
POS	photoreceptor outer segment
ppS	peripapillary sclera
PR	photoreceptor
RGC	retinal ganglion cell
RP	retinitis pigmentosa
RPE	retinal pigment epithelium
SEM	scanning electron microscopy
SPM	scanning probe microscopy
SS	sum of squares
STM	scanning tunneling microscopy
VH	vitreous humour

Chapter 1

Introduction to atomic force microscopy, force spectroscopy, and the eye

1.1 Atomic force microscopy

The early 1980s marked the introduction of Scanning Probe Microscopy (SPM). This was as a result of Rohrer and Binning revolutionizing microscopy through the innovation of the Scanning Tunneling Microscope (STM). The STM initialized this vast and growing type of probe microscopy. It scans surfaces using a sharp probe to sense its structure. It also measures the existing relationship between the probe and the surface. Binning and his colleagues later (1986) introduced Atomic Force Microscopy (AFM), [1] the second SPM type, which was also referred to as scanning force microscopy. AFM is seen as the most versatile of scanning probe microscopes [2]. AFM is a powerful tool, which provides three dimensional information (see Figure 1.1) and high resolution images for the exploration of baseline structures [3, 4]. AFM can run

in almost any environment including aqueous media, which makes it possible to image biological samples under near-physiological conditions [5–7]. Moreover, the mechanical properties of soft and non-homogeneous materials, such as biological samples, can be detected.

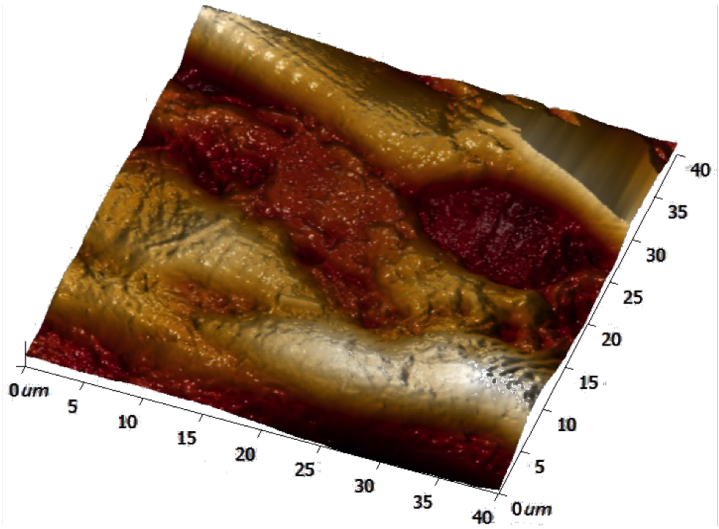

Figure 1.1: 3D-topographic image of retinal layer taken by AFM.

Mechanical motion is among the most significant components of the AFM process. An illustration of a typical AFM investigational configuration is depicted in Figure 1.2. Essentially, the tip has a radius varying from 10 to 50 nm which is located on a cantilever comprised of Si and coated using a reflective covering to accurately detect the movements made by the cantilever [8]. While the cantilever bends with reaction to the surface (as in Equation 1.1 discussed later), the laser beam focused on the back of the cantilever is subjected at varied angles. The photodiode sensor is used to measure such a laser beam in order to estimate its deflection. A typical photodiode applied in AFM experimentations has been illustrated in Figure 1.3. Furthermore, Equation 1.2 (discussed later) expresses the laser beam's deflection intensity. The laser beam's deflection in the current case involves cantilever displacement.

The basic scanning approach involves having the sample raster-scanned engaging

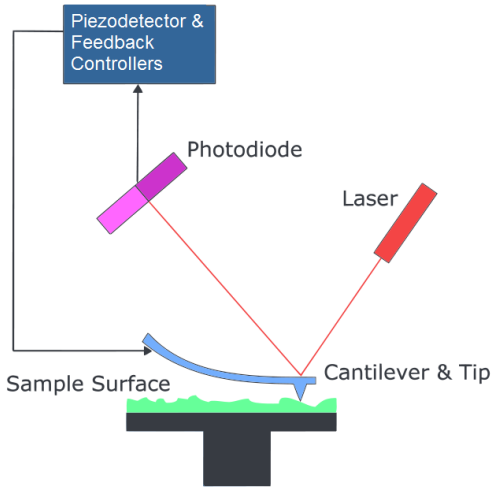

Figure 1.2: Block diagram of an Atomic Force Microscope (AFM). Reproduced under Public Domain from Wikimedia Commons

piezoelectric actuators beneath the sample and within the xy (sample) plane. This movement along the x and y axes is controlled by a piezoelectric actuator with precise control at the length scales measured during a typical AFM experiment [9]. Up and down deflection is felt by the cantilever for the purposes of handling the sample topography. With its operation resembling that of a linear spring, the cantilever engages Hooke's law in determining the force, hence

$$F = -kx \tag{1.1}$$

with k denoting the spring constant of the cantilever, while x denotes the deflection in the surface normal direction [8, 10].

In addition, the reflection of the laser beam is mirrored onto the photodiode detector, as depicted in Figure 1.3. While the tip is scanning the surface some bending of the flexible cantilever is seen in reaction to several repulsive or attractive surface interactions. For such a case, the laser beam's deflection can be used to determine the cantilever's deflection [2, 12]. The deflection signal (DFL) denotes the total deflection

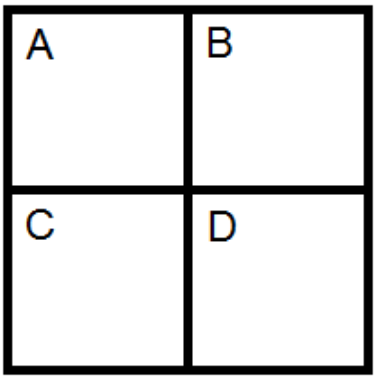

Figure 1.3: Schematic of the photodiode detector. Reproduced with permission from NT-MDT. [11]

intensity while that of detector laser beam for every quadrant is denoted by A, B,C, and D.

$$DFL = (A + B) - (C + D) \tag{1.2}$$

From the DFL, it can be determined whether the cantilever is close to the sample or far from the sample. The feedback loop's sensitivity is set by the user in a criterion that enables the z (surface normal) axis controller to accurately maintain the tip sample's height through tip repositioning.

This overall configuration depicts the basis of AFM investigations with unique modifications being added for further specialized approaches. The interaction forces for all AFM modes are either repulsive or attractive depending on the mode of scanning. These are shown in a force–displacement curve in Figure 1.4. As the distance between the AFM tip and sample decreases, weak attractive forces are generated between tip and sample. As the tip and sample are steadily brought nearer to each other, the attractive forces increase until the atoms become so near that the electron clouds start to repulse each other electrostatically [13].

The AFM can operate in several modes. A further explanation of contact and tapping modes will be given later in this chapter; they are the only modes that were

utilized in this research.

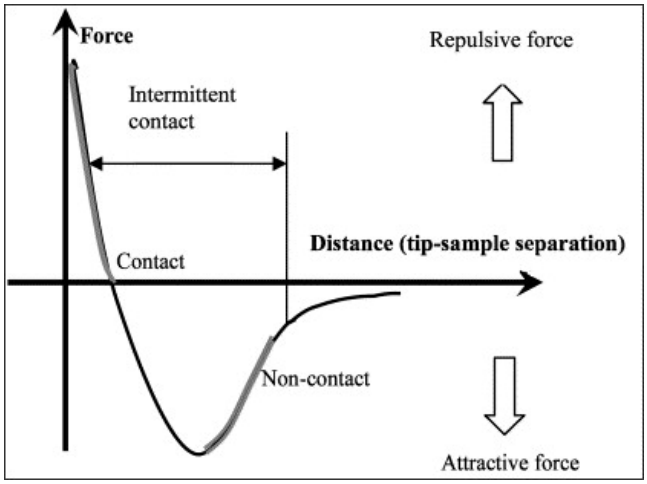

Figure 1.4: Interatomic force difference versus distance (tip-sample separation). [13]

1.1.1 Contact mode in air

Contact mode or repulsive mode is the simplest and oldest AFM mode, and it is appropriate for imaging flat and smooth surfaces [4]. Although our samples for this study were rough and soft, most of the eye images were obtained through contact mode without difficulty. In this mode, the AFM tip is at all times in direct contact with the sample surface. The space between the tip of the probe and the sample surface is of smaller amount than a small number of angstroms (Å). Therefore, the interaction force between the tip and the sample is repulsive in nature. Figure 1.4 shows that the gradient of the curve in the corresponding regime is rather sharp. Thus, the repulsive van der Waals forces constrain all other attractive forces that can be disposed to act [13].

While performing the mapping procedure, there are two possible ways of scanning the sample surface. The surface of the sample can be scanned through contact where scanning of the surface typically involves a constant force or a constant tip height [10].

Surface scanning occurs when the cantilever deflects up and down to accommodate topography under the probe while the feedback loops remain at the same cantilever deflection defined by the user (i.e. imaging force) and at the same time ensures that there is a vertical movement of the tip (in our case) or the sample (for other instruments) using the z-piezoelectric actuator [13]. This change in the cantilever deflection can be monitored by the detector, and the force can be calculated through Hooke's law as Equation 1.1 indicates. The movement of the piezo at each pixel location results in the generation of a high-quality image of the surface (see Figure 1.5 illustrating a height profile of the neurones). While the equipment is in constant height mode, the feedback system is usually switched off to allow the z-height to remain constant during the x-y scanning. At this time, the photodetector values are converted into z values [10, 14].

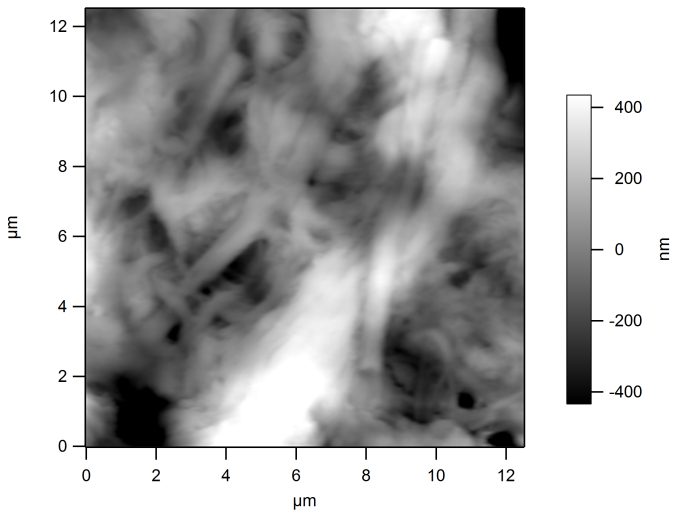

Figure 1.5: Height profile of the neurones taken by AFM contact mode

This method of scanning used is considered appropriate for both wet and dry imaging because it can produce even atomic resolution, but the problem is that it touches the surface. Therefore, contact mode may cause damage to both the sample

and the probe, as is mentioned above. Another problem associated with this mode is the development of lateral forces as the probe moves across the surface [10, 12].

1.1.2 Tapping mode in air

Tapping mode was invented in 1987, and it is an AFM mode which is often used for rough surfaces to reduce specimen damage [4]. The atomic force microscopy tapping mode is a dynamic mode, which involves amplitude modulation for imaging the topography of the sample [15]. This mode oscillates the probe at a certain frequency, which ensures that the sample is touched only at its far end during the probe's downward movement. The oscillation amplitude reduction becomes the outcome control signal that facilitates surface topography measurements [16, 17].

The cantilever-edge movement is associated with elastic responses, hydrodynamic damping with the medium, tip-sample interactions, and excitation force. Thereby, the nonlinear, second-order differentiation equation is as indicated:

$$m\frac{dz^2}{d^2t} = -k_c z - \frac{m\omega_0}{Q} + F_{t,s} + F_0 \cos\omega t \tag{1.3}$$

where f_0 is the amplitude of the driving force, and ω is the angular frequency of the driving force. Q, ω_0, and k_c are the quality factor, angular resonance frequency, and spring constant of the cantilever respectively; $F_{t,s}$ denotes the tip-sample interaction.

The tip-sample geometry is shaped as a sphere (tip) and flat (sample), which has been shown to be a reasonable assumption. The tip-sample interaction derives from attractive and repulsive forces as shown in the following equation:

$$F_{t,s}(z_0, z) = -\frac{AR}{6(z_c + z)^2} \tag{1.4}$$

where A is the Hamaker constant and R is the tip radius. Beside that, the tip-sample distance d is calculated as the sum of the tip-sample rest distance (z_c), and the tip position $z(d = z_c + z)$. The z coordinate is the tip's rest position as illustrated in Figure 1.6 [15].

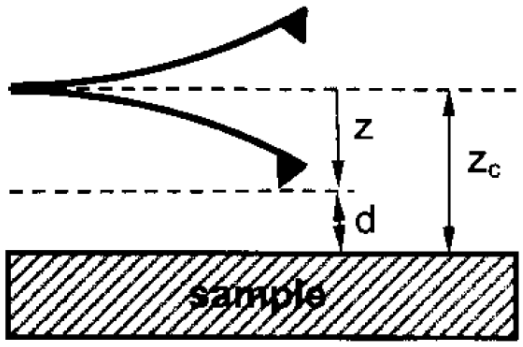

Figure 1.6: Schematic of the tip-sample interaction. The tip-sample distance (d) is the sum of the rest tip-sample separation (z_c) and the z coordinate, where z as defined is a negative number. [15]

Tapping mode provides numerous advantages for imaging biological samples, including the reduction of lateral forces as the probe is in a contact for a small fraction during its tapping movements. Therefore, higher lateral resolution can be obtained [10].

1.1.3 Tapping mode under fluid

Imaging a sample with AFM in liquid can be a challenge. However, it provides significant advantages in biological systems [18]. These advantages include the elimination of capillary forces, the reduction of friction forces, and the limitation of damage to the sample as the sample surface gets softer by adding fluid [19, 20]. Using contact mode to image under fluid often causes damage or deformation of the sample, and to overcome any problems that contact mode may cause, tapping mode is utilized [7].

There exists a noteworthy difference between operating AFM tapping mode in fluid and that in air. The main variance between tapping mode in air and in fluids is seen in the quality factor (Q) of the girder (cantilever). In air, the Q-factor is usually between 200–400, while in fluids it is 1–5 [20]. This is mostly because of the amplified hydrodynamic damping in fluids compared to air [21]. Therefore, the hydrodynamic loading effects are taken into account when tapping mode is used in fluid. Sader in 1998 argued that the overall force working on the cantilever $\hat{f}$ operational in liquid can be separated into two components as seen below:

$$\hat{f} = \hat{f}_h + \hat{f}_d \tag{1.5}$$

where $\hat{f}_h$ is the hydrodynamic loading, and $\hat{f}_d$ is the driving force. By analysing the general form of $\hat{f}_h$ and examining the Fourier transformed equations of motion for the fluid, the evident form of $\hat{f}_h$ is as follows:

$$\hat{f}_h = \frac{\pi}{4}\rho_{liq}\omega^2 b^2 \Gamma \hat{\zeta} \tag{1.6}$$

where ρ_{liq} is the density of the fluid, b is the dominant length scale in the hydrodynamic flow which is the cantilever width for a rectangular beam, Γ is hydrodynamic function, and $\hat{\zeta}$ is the displacement [22, 23].

The second cause of the reduction in the Q-factor is through the large increase in frequency noise. Thus, the viscous damping of the cantilever oscillation in fluid at a resonance frequency is described as following:

$$\rho S\frac{\partial^2 \zeta(x,t)}{\partial t^2} + EI\frac{\partial^4 \zeta(x,t)}{\partial t^4} = f_h(x,t) + f_d(x,t) + f_{ts}(Z_c - w(L,t)) \tag{1.7}$$

where ρ is the density, S is the cross section, E is the Young's modulus, and I is the

moment of inertia of the beam. The f_h and f_d terms are forces acting on the cantilever as it is described in Equation 1.5 [23], z_c is the sum of the tip-sample rest distance in Figure 1.4, and f_{ts} is the tip-sample force, which is discussed in the equation below 1.8 and 1.9.

Besides the Q-factor that causes the difference between operating tapping mode in fluid and in air, the tip-sample interaction forces (f_{ts}) also play a role in this difference. Before contact, the tip-sample interaction forces (f_{ts}) are described by the Derjaguin-Landau-Verwey-Overbeek (DLVO) theory for the f_{ts} of a spherical tip and a flat elastic surface as follows:

$$f_{ts}(d) = F_{DLVO}(d) = \frac{4\pi R_t}{\epsilon\epsilon_o K_d}\sigma_t\sigma_s e^{-K_d t} - \frac{AR_t}{6d^2} \tag{1.8}$$

where R_t is the the tip radius, ϵ the dielectric constant of the medium, ϵ_o the permittivity of free space, K_d the Debye length, σ_t and σ_s the surface charge density of the tip and sample, A the Hamaker constant between the tip and the sample material, and d is the instantaneous tip-sample separation. After contact, tip-sample interaction forces (f_{ts}) are described by Derjaguin-Muller-Toporov (DMT) contact mechanics for the same case as given:

$$f_{ts}(d) = F_{DMT}(d) = \frac{4E'\sqrt{R_t}}{3}(a_o - d)^{\frac{3}{2}} + F_{DLVO}(a_o) \tag{1.9}$$

where E is the effective Young's modulus of the tip and the sample material, and (a_o) is the intermolecular distance [21].

1.2 Force Spectroscopy

Apart from imaging, force spectroscopy is noted as a significant application of atomic force microscopy, which adapts the atomic force microscopy from high resolution imaging to a measuring tool [17, 24]. Rather than scanning the probes in y and x directions, the force curve is facilitated by observing the cantilever deflections because of the vertical displacements of the specimen or tip [17]. The force curve does not only facilitate information about the van der Waals forces [25] and adhesion forces [26] but also provides complex information about the plasticity and elasticity of the of the substance. As such, one can map mechanical information by interaction force measurements using atomic resolution [27]. Figure 1.7 illustrates a force curve obtained from an indentation experiment involving the eye specimen, demonstrating the approach and retract phases.

The vertical axis in a force curve plot presents cantilever deflections, which provide interaction force measurements as a function of tip-sample separation presented along the horizontal axis [28, 29]. At the initial stages of the approach phase, the tip is kept off the surface of the sample. Therefore, no interaction between the sample and the tip is observed. When the tip approaches the sample surface, the minimal range interactions between the two can be measured, and the force of attraction makes the tip jump and come into contact (jump-to-contact distances are significant parameters for calculations) [24]. The tip penetrates the sample surface until it comes to the desired point, which serves as a trigger point, which is defined before commencing the experiment (I use 5.0 nN for minimal sample damage).

Afterwards, the tip gradually starts pulling away from the sample. However, because of the adhesion between the sample and the tip, the tip does not immediately pull back from the sample, the force used becomes stronger than the adhesion energy, and the cantilever tip jumps off-contact, which is another significant parameter.

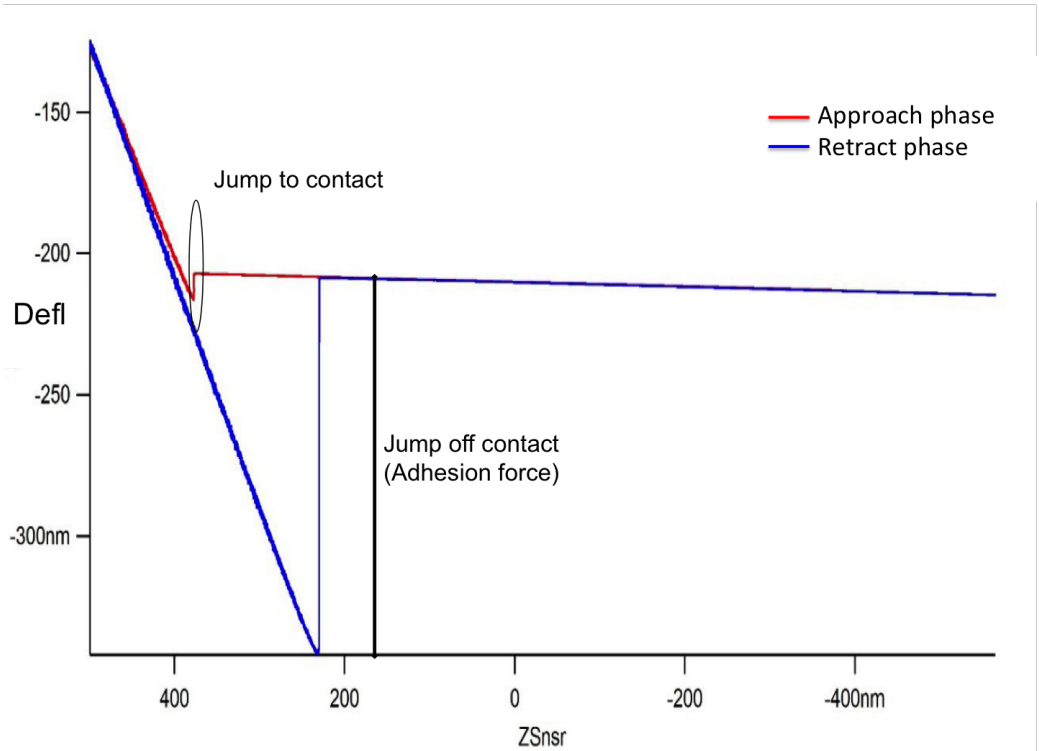

Figure 1.7: Typical force curve showing both the approach (red line) and the retract (blue line) phases.

Through analysing the approach line of the force curve, the mechanical properties such as stiffness of the sample (and therefore Young's modulus) can be obtained. Moreover, the area between the negative part of the withdrawal curve and the horizontal axis can provide information about the work of adhesion.

Young's modulus E, which is sometimes referred to as the elastic modulus of a material, is an important numerical characteristic of materials. It is the ratio of stress in pascals (force per unit area) over strain (proportional deformation), which is dimensionless, as is indicated in the equation below [30, 31]:

$$E = \frac{stress}{strain} \tag{1.10}$$

This numerical value is critical for observing changes in cells during cell division or on adding drugs to the cells [32]. It is also important to be known for designing artificial tissues to match those of the native tissue [33]. The Young's modulus can be calculated from the slope of the withdrawal part of the force curve, as is mentioned above, by fitting one of the appropriate contact mechanics models [10]. These models can be classified into two forms: nonadhesive methods and adhesive methods.

1.2.1 Analysis models

1.2.1.1 The Hertz model

The Hertz model is the most used model compared to other models used for contact mechanics [34]. This model established the relationship between the size and shape of the bodies of contact derived from the elastic deformation of these bodies [35, 36]. Typically, when a spherical probe indenting a spherical specimen, the force depth can be determined for a small deformation by the Hertz model equation as follows:

$$F = \frac{4E^{*}\delta^{\frac{3}{2}}\sqrt{R}}{3} \tag{1.11}$$

Hertz, in 1882, raised the importance of relating the radius of the circle of contact a to the load (F), the spherical indenter radius (R), and the elastic properties of the contacting material (see Figure 1.8) by:

$$a^{3} = \frac{FR}{E^{*}} \tag{1.12}$$

where E^{*} is the effective Young's modulus of the indenter tip and the sample described

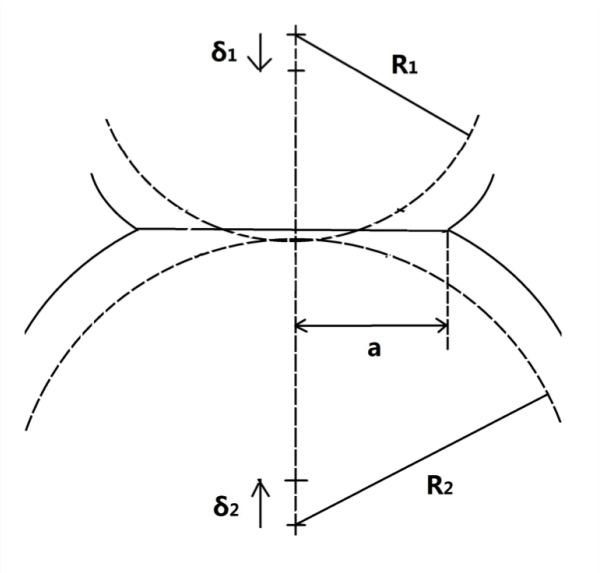

Figure 1.8: Schematics of the contact area between two spheres where the two spherical indenters are described by a radius R_1 and R_2, and the radius of the circle of contact is described by a. δ_1 and δ_2 are sphere 1 and 2 displacements [37].

by:

$$\frac{1}{E^*} = \frac{4}{3}\left(\frac{1-\nu_1^2}{E_1} + \frac{1-\nu_2^2}{E_2}\right) \tag{1.13}$$

where E and ν are the Young's modulus and the Poisson's ratio of the material, respectively, and as the contacting bodies are spheres with radii R_1 and R_2 then R is the tip curvature radius presented as [35, 38]:

$$R = \frac{R_1 R_2}{\left(R_1 + R_2\right)} \tag{1.14}$$

The Young's modulus of the force-distance curve can be calculated through the reduction equation of the Hertz model for spherical probe indenting soft specimen as given below:

$$F = \frac{4E\delta^{\frac{3}{2}}\sqrt{R}}{3(1-\nu^2)} \tag{1.15}$$

where δ is the measured indentation (in meters) [35].

The Hertz model is suitable for only homogeneous, isotropic, and linear elastic materials that show no attractive surface forces (adhesion) [39] as it is shown in Figure 1.9. These restrictions limit the utility of the Hertz model. Therefore, other models have been developed to overcome these restrictions to be suitable for more specific conditions [40]. For example, force curves obtained in air show a strong adhesion force as the tip pulls back from the sample during the retract phase as is indicated in Figure 1.7.

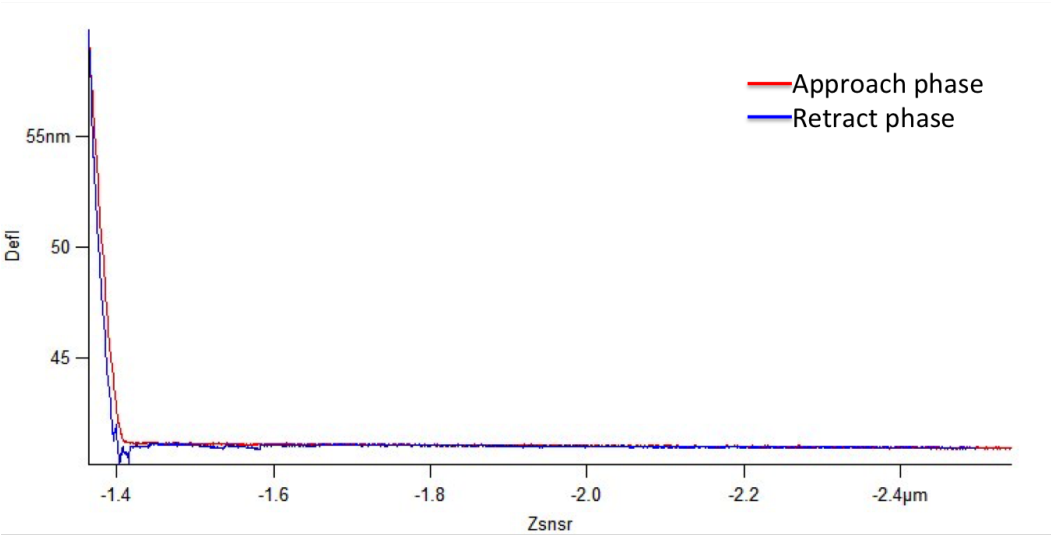

Figure 1.9: Force-distance curve.

1.2.1.2 The JKR model

The short-range adhesive force in Hertzian contact was added by Johnson, Kendall, and Roberts in the 1990s which leads to the power of the JKR theory [35]. This model considers the adhesion force between two spheres in the contact area, so the contact between them is shown in Figure 1.10. Thus, the JKR model correlates the adhesion force (F) with the work of adhesion $\Delta\gamma$ through the following equation:

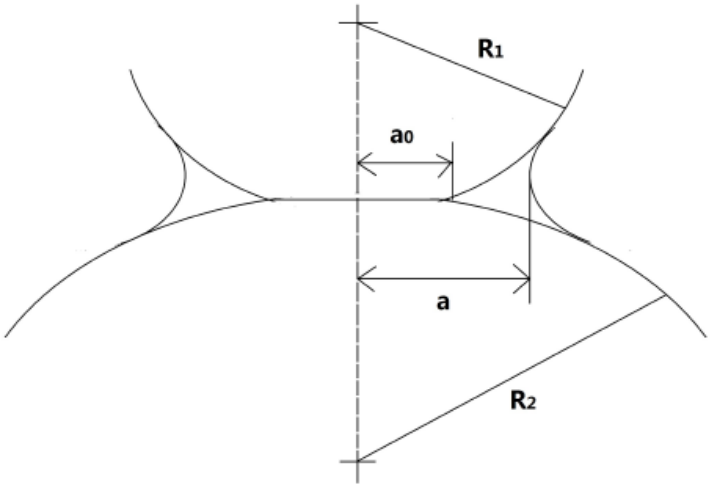

Figure 1.10: The JKR model includes a short range of adhesion in the contact area between two spheres resulting in larger contact radius a than the one determined from the Hertz model (a_0) [37].

$$F = \frac{3}{2}\pi\Delta\gamma R \tag{1.16}$$

where R is the tip radius and the work of adhesion is given by:

$$\Delta\gamma = \gamma_1 + \gamma_2 - \gamma_{12} \tag{1.17}$$

The surface energy of the materials of spheres 1 and 2 are γ_1 and γ_2, respectively, and γ_{12} is the interfacial energy [35, 38, 41]. Also, the contact radius at zero load a_0 was concluded to be the following:

$$a_0 = \left(\frac{6\pi\Delta\gamma R^2}{K}\right)^{\frac{1}{3}} \tag{1.18}$$

1.2.1.3 Minimal indentation model

The JKR equation was adapted by Dr. Chuan Xu, who was a PhD student in Dr. Merschrod's group at Memorial University of Newfoundland, to be suitable for calcu-

lating the Young's modulus of soft materials at a minimum indentation depth. The minimum depth depends on the material properties, which should be less than 10 nm [37]. Many advantages can be considered for using this method for soft materials including biological samples. This method is less destructive to the sample when the integrity of the sample is important in the study [42]. It also can minimize the viscoelastic response of the material [43].

Under these considerations, the Young's modulus of the materials that is calculated through the minimum indentation JKR depends on two important parameters. These two parameters were discussed in the force spectroscopy section (1.2), which are the jump to contact and jump off contact of the sample surface. Both of these parameters can be extracted from the force curve in order to obtain the Young's modulus of the material easily. Thus, the final expression of the minimum indentation JKR to calculate the Young's modulus was presented as the following:

$$E_s = \frac{5}{2} \mid F_p \mid R^{\frac{1}{2}}(1-\nu_s^2)\left(\triangle d - 2\left(\frac{AR}{24k}\right)^{\frac{1}{3}}\right)^{\frac{3}{2}} \tag{1.19}$$

where F_p is the jump-off contact force (jump-off contact $\times k$ spring constant), R is the indenter diameter (which depends on the tips that are used), ν_s is Poisson's ratio for the material, Δd is the jump-to-contact distance, and A is a constant which is equal to 0.165 nm [37].

1.3 The eye

The eye is lauded as an important organ that facilitates visual sensitivity in many organisms [44]. The major function of the eye is conversion of light into nerve signals and then sending the signals to the brain through the optic nerve. The structure of

the eye is shown in Figure 1.11.

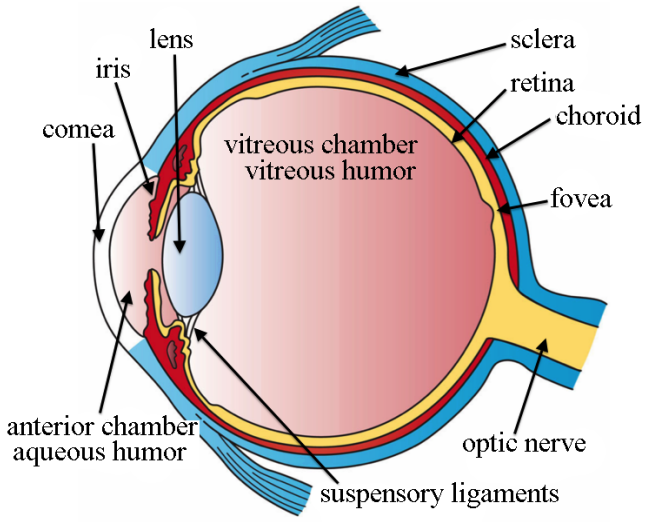

Figure 1.11: The basic structure of the eye, labeling its main features. Reproduced under Public Domain from Wikimedia Commons

The eye is an embryologic extension of the nerve system, and shares various common physiological and anatomical features of the cognitive system. The eye and the brain enjoy the protection of the skull walls, and both possess coverings composed of fibrous materials. Like cognitive system, the eye has a double blood circulatory system that serve the critical nervous layers in the retina [45]. Eyes primarily consist of triple layers, triple compartments, and triple fluid layers. The triple compartments consist of the external fibrous layer, the vascular middle layer, and the nervous inner layer. The fibrous layer is composed of the sclera lamina crib Rosa, and cornea. The second vascular layer is composed of the choroid, ciliary body, and iris. The third nervous layer is composed of the retinal photoreceptors, and pigment epithelium of the retina. The retinas facilitate the eye focus. Additionally, the three layers are the back and front compartments, and the vitreous compartment. The triple fluids include blood, vitreous humour, and aqueous humour. Notably, compartments, layers,

and fluids facilitate significant roles in the visual process.

1.3.1 The retina

The retina is a light-sensitive layer which lines the inner surface of the eye [46]. It is involved in the central nervous system, and is exposed regularly to various kinds of mechanical stress. The retina is known as "the photographic film" of the eye as this layer converts light to nerve signals, transmitting them to the brain [47]. The retinal tissue mainly consists of three layers, which are the inner retinal neurons, photoreceptors, and pigment epithelium cells (PE) as demonstrated in Figure 1.12, which was taken by Dr. Robert Gendron who provided us with eye samples from the Faculty of Medicine at Memorial University.

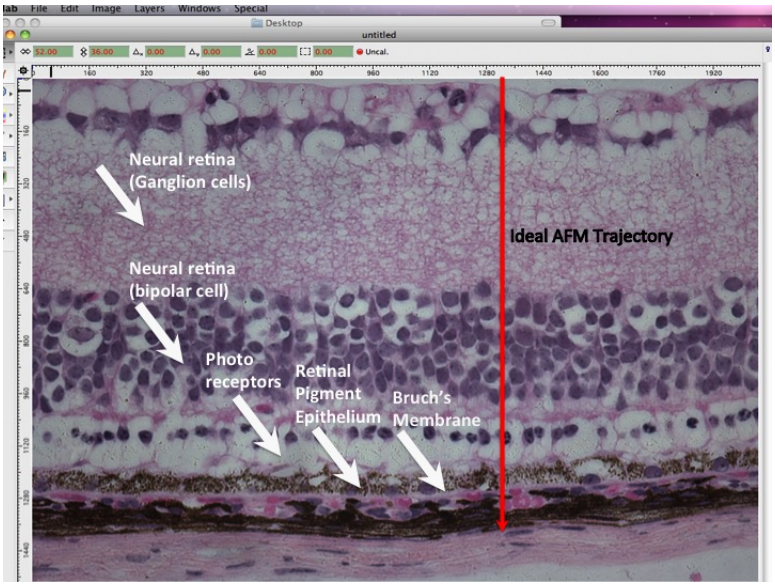

Figure 1.12: Optical microscopic image of retinal tissue illustrating the four main layers: the inner retinal neuron layers (ganglion and bipolar cells), photoreceptor cells, and the retinal pigment epithelium. The ideal AFM trajectory that was followed in imaging and measuring the mechanical properties of retinal tissue are shown by the arrow. Taken by Dr. Robert Gendron.

The inner retinal neuron layers consist of definite neuronal cell types, including

bipolar, horizontal, amacrine, and ganglion cells. The inner neurons are similar to brain neurons featuring typical neuronal morphology and functions. Both ganglion and bipolar cells mainly function in signal transformation to the brain, whereas horizontal and amacrine cells function in integration and modulation signals. The bipolar cell also forms the prime link between the ganglion cells and the photoreceptors [48].

The photoreceptors in the retina consists of two types of cells: rods and cones. Rod cells are responsible for poor light vision (scotopic) and are sensitive to very small amounts of light. However, cone cells are responsible for colour and day-time vision (photopic) and react to strong light [45, 49]. This is because the outer segment of the rod is longer and holds more photopigment that the cone [49]. In some species, this layer can form up to 40% of the retinal tissue [50]. Photoreceptor cells, the rod and cone cells, are responsible for the transformation of light into neural signals [51].

Finally, the retinal pigment epithelium (RPE) is a single layer of pigmented cells that lies between the outer segments of the retina, which are the photoreceptor cells, and the Bruch's membrane [52]. The RPE cells are rich in organelles including lysosomes, mitochondria, and pigment granules [48]. The tight junctions and the adherens connect the RPE cells tightly and play a vital function in the role of RPE cells as blood and retinal barrier component. RPE is essential for the health, survivability, and the functioning of the overlying retinal photoreceptor cells due to its highly metabolic cell nature [53]. Researchers estimate that about 20 photoreceptor cells make contact with a single RPE cell [54]. Some of the functions of the RPE cells include the transportation of nutrients, the secretion of growth factors, the absorption of the stray light, retinol recycling, especially during the visual cycle, and phagocytosis of the debris of the photoreceptor outer segment (POS) which are shed on a daily basis by the retinal cone and rod cells [53].

1.3.1.1 Retinal diseases

The majority of the diseases that affect the functionality of the retina are of the degenerative type. Retinal degeneration implies that the retina cells die gradually. Retinitis Pigmentosa (RP) is a typical eye disease that results from the degeneration of the retina. RP is a form of retinal disease that involves a combined set of other retinal diseases, some of which may be inherited. RP affects more than 200,000 Americans and millions of others in the world [55]. RP leads to the death of the rod cells that are critical for night vision, resulting in a situation where the affected person is blind at night [51]. The death of the rod cells eventually leads to the loss of the mid-peripheral field [56].

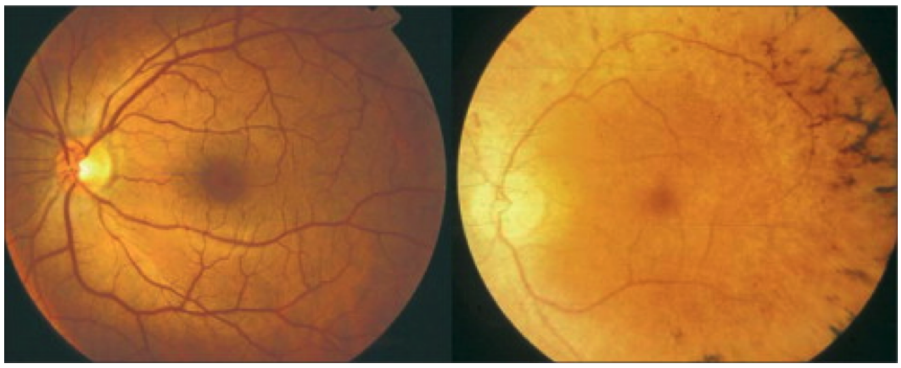

Figure 1.13: Healthy eye (left) and an eye with retinitis pigmentosa (right) [57]

The retina is also affected by another form of degeneration known as Macular Degeneration (MD). Due to the contribution of age to MD, it is popularly known as age-related macular degeneration (AMD) [53]. For people aged more than 50 years, AMD is the major cause of the loss of sight. With age, acellular polymorphous debris is centrally deposited between the Bruch's membrane and the RPE. AMD affects the macular part of the retina that is located behind the retina and sandwiched between the RPE and the choroid [58,59]. The photoreceptors densely populate the macula to

allow it to provide very high-resolution visual acuity so as to permit an individual to view very minute details and have facial recognition ability [60]. Due to the numerous functions that the RPE cells play, the macular portion of the retina degrades due to being subjected to daily stress such as light absorption, phototoxicity, heat stresses, and other damages from oxidation.

The development of AMD is accelerated by changes in the Bruch's membrane and the RPE due to age and toxicity. The earliest signs of the macular degeneration are evident by the deposition of drusen, an abnormal extracellular material, between the RPE and the Bruch's membrane [53]. In advanced stages, AMD is categorized into two types: Dry AMD and wet AMD, as is shown in Figure 1.14. Dry AMD is also known as geographic atrophy while wet AMD is referred to as neovascular AMD. Dry AMD is characterized by the appearance of the progressive atrophy of the choriocapillaris, the RPE, and the photoreceptors. On the other hand, neovascular AMD is characterized by the breakage of the choroidal neovascularization up to the retinal region resulting in the leaking of lipids, fluids, and blood in addition to fibrous scarring [61].

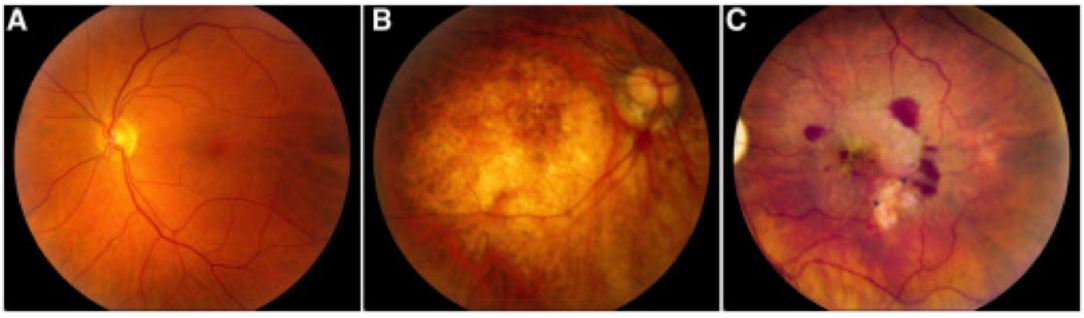

Figure 1.14: The ocular fundus of (A) a healthy eye illustrating the normal pigmentation and blood vessels, (B) the late-stage of dry AMD showing large regions of depigmentation, particularly in the macular, and (C) wet AMD, showing leaky blood from the choroid through the retina [62].

1.3.1.2 The Bruch's membrane

The Bruch's membrane is associated with age-muscle degeneration challenges. It has been observed that inner and outer collagenous surfaces undergo age-associated changes [63]. The collagenous membrane is elastic in nature, measuring 2 to 4 micrometers thick and located in between the choroid Bruch membrane, and the retinal pigment epithelium [64, 65]. The collagenous membrane encompasses five varied layers. The layers include the inner collagenous zone, the retinal pigment epithelial, the elastic zone, the outermost basement, and the outer zone of the collagen surface. The collagen membranes play a significant role because they facilitate the metabolic function in the eye and between the choroid and retina. The collagen membrane also plays the role of simplifying the attachment of retinal pigment epithelial. As such, mapping the mechanical features and the structure of the collagen membrane is a crucial step for better understanding age-associated muscular degeneration [66].

1.4 Thesis summary

This thesis presents AFM and force spectroscopy measurements on eye tissue. Chapter 2 represents a complete AFM mapping of the eye for two different species. Both samples show changes in morphology from one spot to another. In the third chapter, the Young's modulus was measured along the retinal tissue and compared for dry and hydrated samples. Chapter 4 concludes all the work in the previous chapters and outlines numerous suggestions for future work.

The first appendix presents a novel technique called force scanning that was developed previously to quantitatively measure the stiffness. This simple method is used in this thesis to determine the stiffness of this complex tissue and supports the Young's modulus values. The second appendix presents new data on the choroid, which is a

layer that lies on one side of the retina. As this tissue is associated with many diseases that affect the retina, both the topography and mechanical response were measured. Finally, the third appendix presents two different statistical tests that were used to test the variation between the dry and hydrated samples.

Chapter 2

Comparative atomic force microscopy imaging of mouse and fish eyes

2.1 Motivation

Numerous diseases affect the eye and as people age these diseases may lead to serious problems including blindness. Examples of diseases affecting people globally are age-related macular degeneration, diabetic retinopathy, and glaucoma [67, 68]. Most of these diseases cause structural changes in the eye [44]. Figure 2.1 shows how glaucoma thickens the optic nerve and the retina. However, light microscopic images taken on such a large scale do not give sufficient detail to understand the form and function of the underlying eye tissues. Therefore baseline data of healthy eyes in a small scale is needed.

Techniques used to map the morphology of biological samples including the eye are optical coherence tomography, optical microscopy, electron microscopy, and atomic

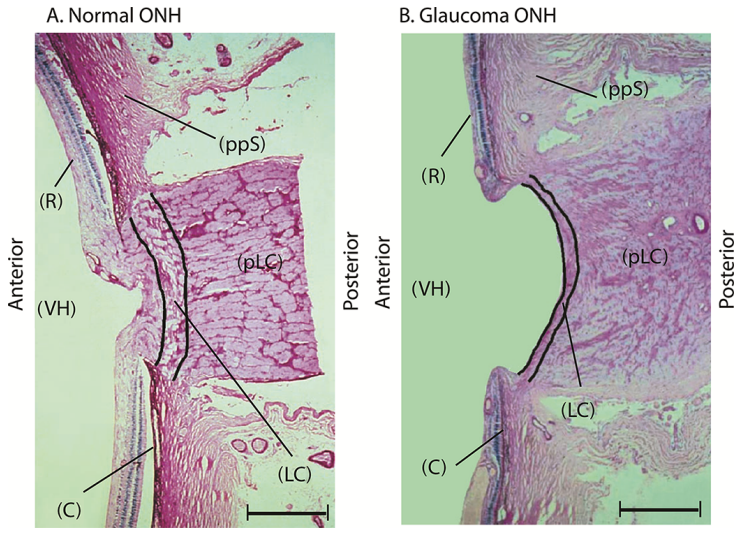

Figure 2.1: Light microscopic image of a normal eye (A) and an eye with glaucoma (B). Presenting retina (R), the choroid (C), the peripapillary sclera (ppS), the lamina cribros (LC) (outlined in black), the post-laminar tissue of the optic nerve (pLC), and the vitreous chamber inside of the eye (VH). The scale bar is 0.75 mm [44]

. .

force microscopy. Optical coherence tomography is used to image the eye as it reaches a resolution of 10 μm [69]. To enhance the standard optical coherence tomography, high-speed ultrahigh-resolution optical coherence tomography is used to achieve a resolution of 2 μm [70, 71]. Optical microscopy is another technique used, reaching a limit of 0.1 μm [72]. Electron microscopy (scanning electron microscopy (SEM) for instance) has also been utilized in many studies to image a biological sample as it reaches 5 nm. Despite the high resolution that electron microscopy can provide, it requires placing the sample in a stable vacuum for imaging [2], and the sample needs to be coated with conductive materials that can chemically alter it. Therefore, mechanical properties can not be obtained directly [73].

Atomic force microscopy (AFM), the technique used in this study for imaging biological samples, is a powerful tool for obtaining high-resolution images as it reaches up to 0.1 nm lateral resolution and 0.1 nm in the z direction (surface normal). It can also provide three-dimensional information to explore the baseline structures of biological

samples [2]. Additional advantages of using AFM for imaging include the ability to prepare the sample without staining or coating, and to measure the mechanical properties directly [66]. However, the majority of previous works using AFM have focused on the cornea [74–76]. These works have used AFM to obtain topography images and mechanical property measurements [77–79].

My work represents the first and therefore a baseline structure of a cross-section of a normal eye for two different samples: rainbow smelt and mouse eyes. This works provides a complete eye mapping on the nanoscale.

2.2 Experiment

2.2.1 Frozen sectioning

Eyes from fully-grown C57.0/B6.0 *Mus musculus* mouse and fully-grown *Osmerus mordax* rainbow smelt acclimatized at a varying temperature (as expounded by Gendron in his paper [80]) were preserved in an Optimal Cutting Temperature compound, as explained in [80]. The preserved specimens were divided into 7.0 μm thick at central retinal level, front, and back orientation facilitated by Leica CM1900.0 cryostats. The frozen specimens were dried in the air overnight before being put under preservation at –80.0 °C. The issues of drying the sample will be discussed in a later chapter in Section 3.3.2. The pieces were frozen and dried in the air rather than preserved with fixing agents to facilitate atomic energy microscopy measurements. After bringing the samples to room temperature, the desired atomic force microscopy trajectories were marked on the underside of the slides on which the samples were mounted. The specimens utilized in this work all meet the protocols set by Memorial University's Institutional Animal Care Committees and extraction was conducted by or supervised by Drs. Driedzic, Paradis, and/or Gendron.

2.2.2 Imaging in air

Atomic force microscopy was utilized for topographic imaging in air. All AFM data were collected using the MFP 3D instrument (Asylum Research, Santa Barbara, CA). For all the experiments, silicon cantilevers coated with gold and chromium having a typical spring constant of 0.1 N/m to 0.3 N/m (purchased from μmasch (HQ:CSC37/Cr-Au)) were used. The spring constant and resonant frequency of each individual cantilever were calculated through the thermal calibration method [81]. Experiments were completed under ambient conditions (using a dehumidifier to maintain the humidity at 30-35%). Images were obtained through contact mode.

To obtain a full mapping of the eye using AFM, eye cross-section samples of rainbow smelt (*Osmerus mordax*) and mouse (*Mus musculus*), which are 5 μm thick, were taken and imaged. The microstructural mapping was begun from the front of the eye (the cornea) to the back of the eye (the optic nerve) as indicated in Figure 2.2, which shows only the rainbow smelt eye. The whole mapping of the rainbow smelt eye took 27 hours to be completed, and 24 hours for the mouse eye. Each image was 90 $\times$ 90 μm in size with a resolution of 256×256 pixels, moving the stage only 80 μm to have an overlap between each image. Moreover, as we were imaging a heterogeneous sample and large area, images were taken at scan rate of 0.5 Hz. All images that are presented in this work are the original images that were obtained directly by AFM without any modifications.

2.3 Results and discussion

A cross-section of rainbow smelt *Osmerus mordax* and *Mus musculus* mouse eyes were imaged using a high resolution technique (AFM) in order to obtain full mapping

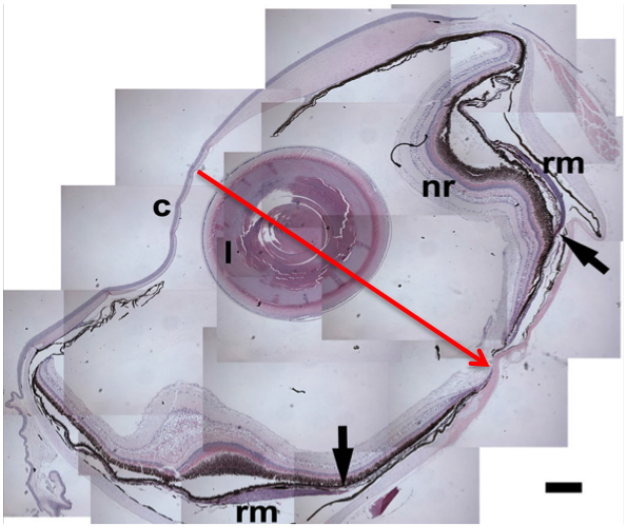

Figure 2.2: A cross-section of the whole rainbow smelt (*Osmerus mordax*) eye showing the cornea (c), lens (l), neural retina (nr), and rete mirabile (rm). The scale bar for the image is 400 μm [80]. The arrow indicates the trajectory that we followed for mapping the whole eye starting from the cornea to the optic nerve.

of the eye. The same image procedure was followed to image both eyes. A set of images were collected from both samples and each image was 90 $\times$ 90 μm. Figure 2.3 illustrates six height images taken from the front, middle and back of the rainbow smelt eye sample. The images show the complexity of the eye as it can be observed that some of them – for example, images a, b, and d – consist of multilayer.

The complexity and variability made it difficult to identify some layers when they were compared to microscopic images. Therefore it should be mentioned that only an area in the back of the eye, which is shown in Figure 2.4, was definitively assigned after consulting with Dr. Robert Gendron. This area represents the vascular layer of the eye in a general term, which are either the blood vessels of the retina or the choroid as both consist of the blood vessels system. Furthermore, after imaging the back area multiple times, we concluded that this area specifically represents the blood vessels of the retina. The depth of the pore was measured through taking the section across of this particular area, as demonstrated in Figure 2.5, where the height trace

(bottom figure) correlates to the topographic image above it. The trace shows that the depth of the pore in the image of the rainbow smelt was about 790 nm.

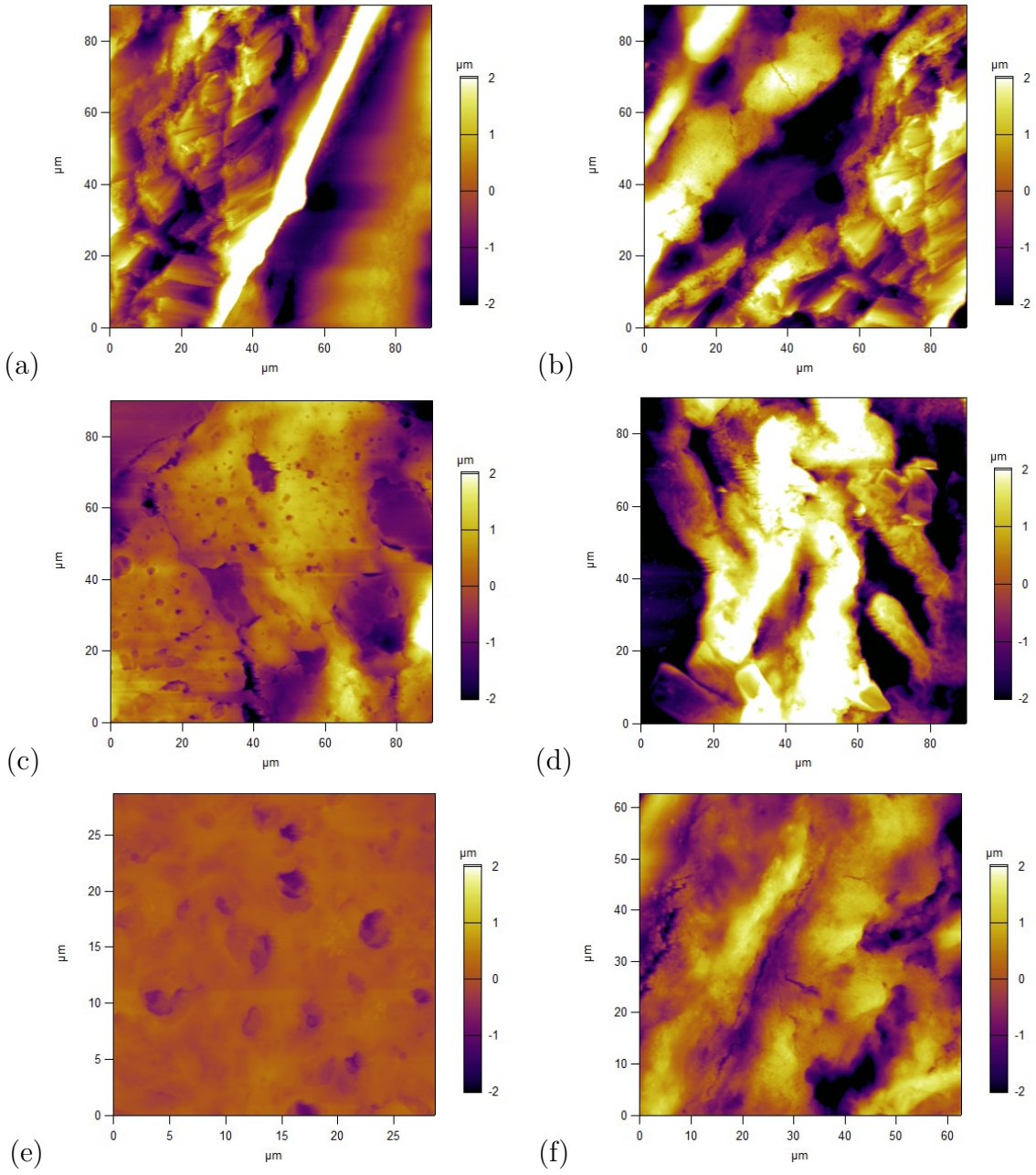

Figure 2.3: Height topography images of the rainbow smelt eye representing a unique part of the eye in each image: (a,b) front, (c,d) middle, and (e,f) back of the eye. They are all 90 × 90 μm with a height scale (indicated by colour) of 4 μm.

The purpose of mapping the eye was to identify the layers by AFM, but as the

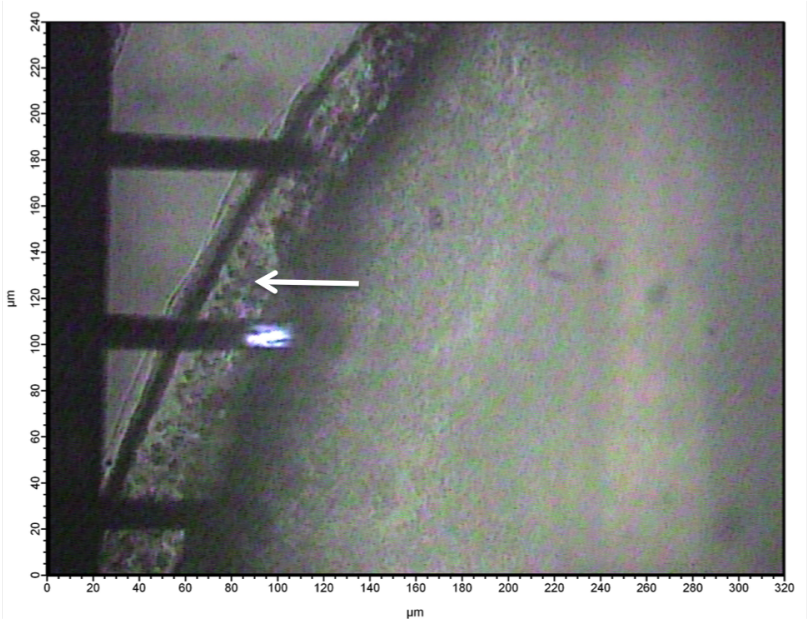

Figure 2.4: Captured image from the AFM camera. The arrow points at the area (blood vessels) that was distinguishable from the back of the eye.

layers were not distinguishable in the rainbow smelt eye, the mouse eye was mapped. Figure 2.6 illustrates another six height images of the mouse eye where the main features of the eye are presented. Based on the images that we obtained, we correlate them with their function. For example, the cornea is considered to be a fibrous layer, and image (a) in Figure 2.6 is evidence for that. Also, retinal blood vessels, which are illustrated in image (e), appear as deep pores similar to retinal blood vessels of the rainbow smelt eye that is shown earlier in Figure 2.5, presenting the depth of the pore. Image (e) in Figure 2.3 and image (e) in Figure 2.6 are taken from the same area, but they do not have to be exactly the same as each of them were taken from different samples. Thus, the structure of the blood vessels may vary from one sample to the other, and with species.

To identify the main features in the mouse eye, several techniques were performed. These techniques include using the optical microscopic image of the whole eye, which is shown in Figure 2.2, to identify the sample imaging location in both the optical

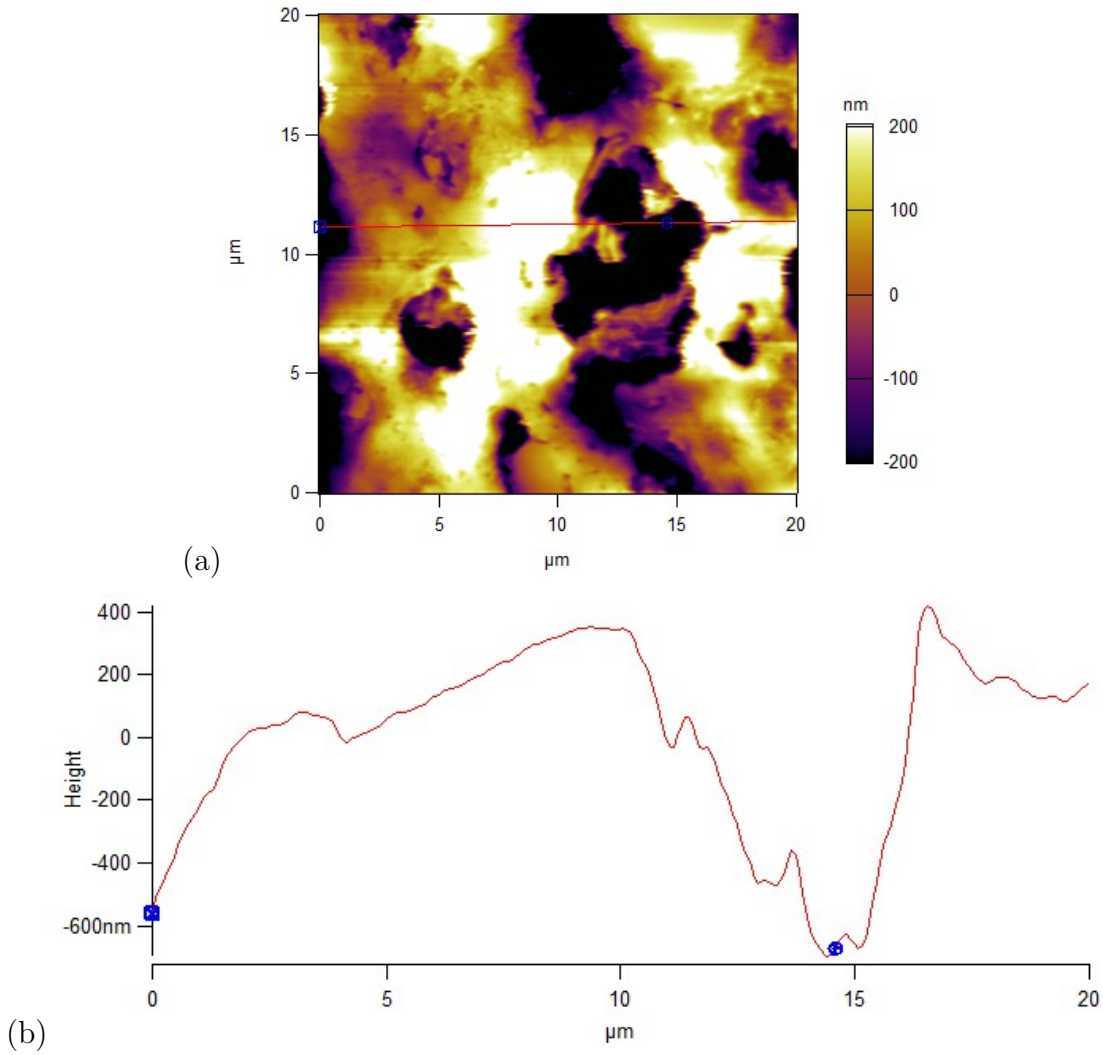

Figure 2.5: (a) 20 × 20 μm AFM topography image of retinal blood vessels obtained from the rainbow smelt eye. (b) Cross section profile of the above topographic image showing the depth of the pore.

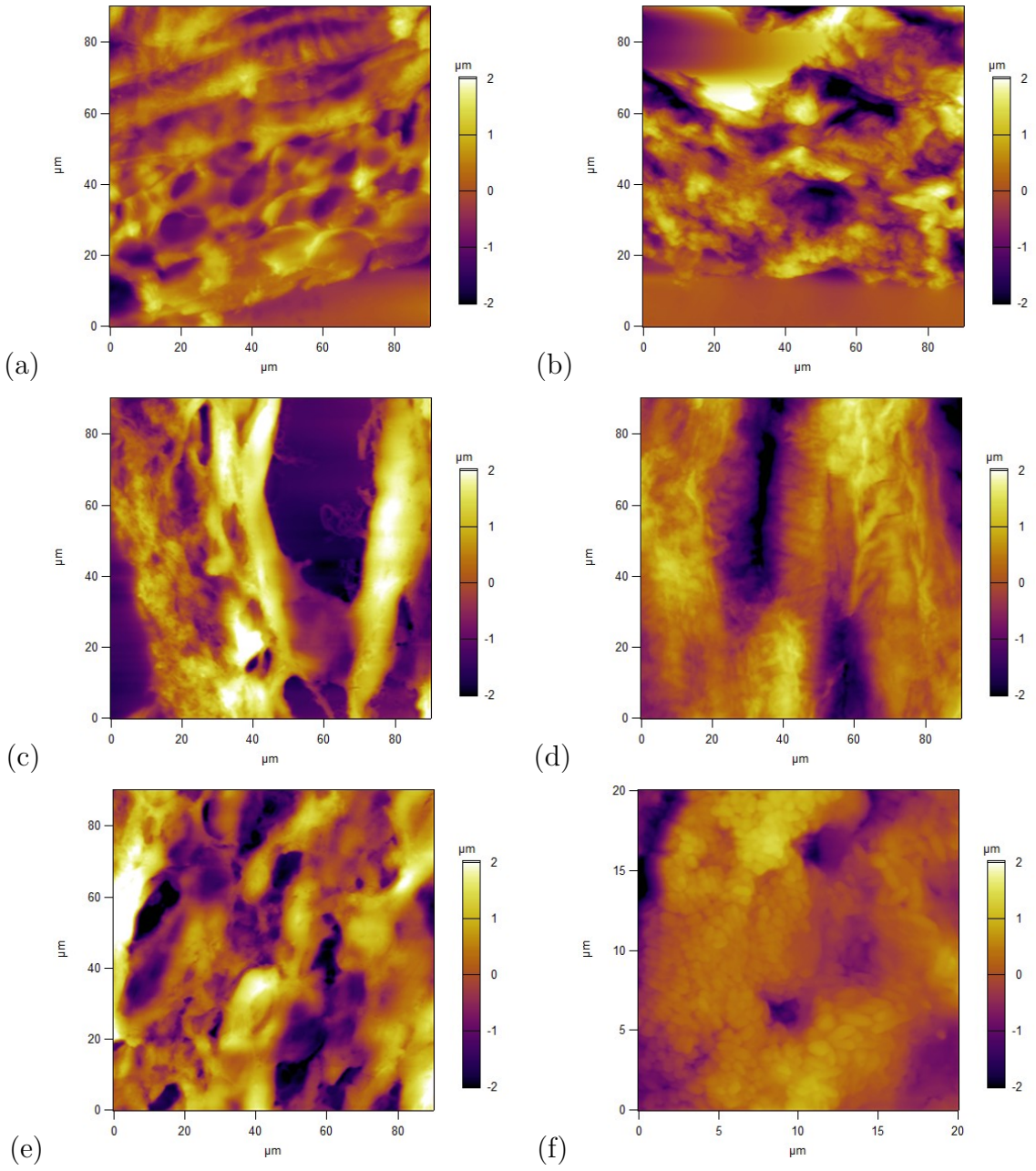

Figure 2.6: Height topography images of mouse eye representing a unique part of the eye in each image: (a) cornea, (b) iris, (c) lens (d) vitreous humor (e) retinal blood vessels, and (f) choriocapillaris. Images are 90 × 90 μm with a vertical scale (indicated by colour) of 4 μm.

microscope and the AFM, to correlate between those sources of data. However, we were imaging the eye with a small scale by AFM, with images of 90 μm across and less, while the optical image is 400 μm across. Therefore it is really hard to compare such a small scale with a large one.

Another technique was used to identify features of the eye: scratching the sample with the AFM and staining it later to correlate the position with the optical microscopy. To do this, various AFM tips with different spring constants were used. We expected the tissue to be soft enough to be scratched immediately with a stiff tip, but unfortunately we could not scratch it. By luck, an accidental scratch did occur along the retina by a glass slide, and those optical microscopic images will be presented in the next chapter.

Finally, imaging the mouse eye multiple times and correlated features with their functions appeared to be the best techniques to identify the main structure of the eye. In this way we could examine the extent of heterogeneity between different images and identify the characteristic features of each region.

2.4 Conclusion

Having a complete mapping of the eye from the cornea toward the optic nerve leads to the importance of understanding the eye structure beyond the optical microscope. This accumulation of AFM images across the whole eye has been achieved for the first time. Although that these microstructural images of some parts of the eye, obtained from rainbow smelt, were not identified by correlating them with microscopic images, this mapping built the investigations of unique studies. One of these studies is the comparison of cold and warm vascular regions of rainbow smelt, which is the only area that is identified in the back of the eye. This research was accomplished by a

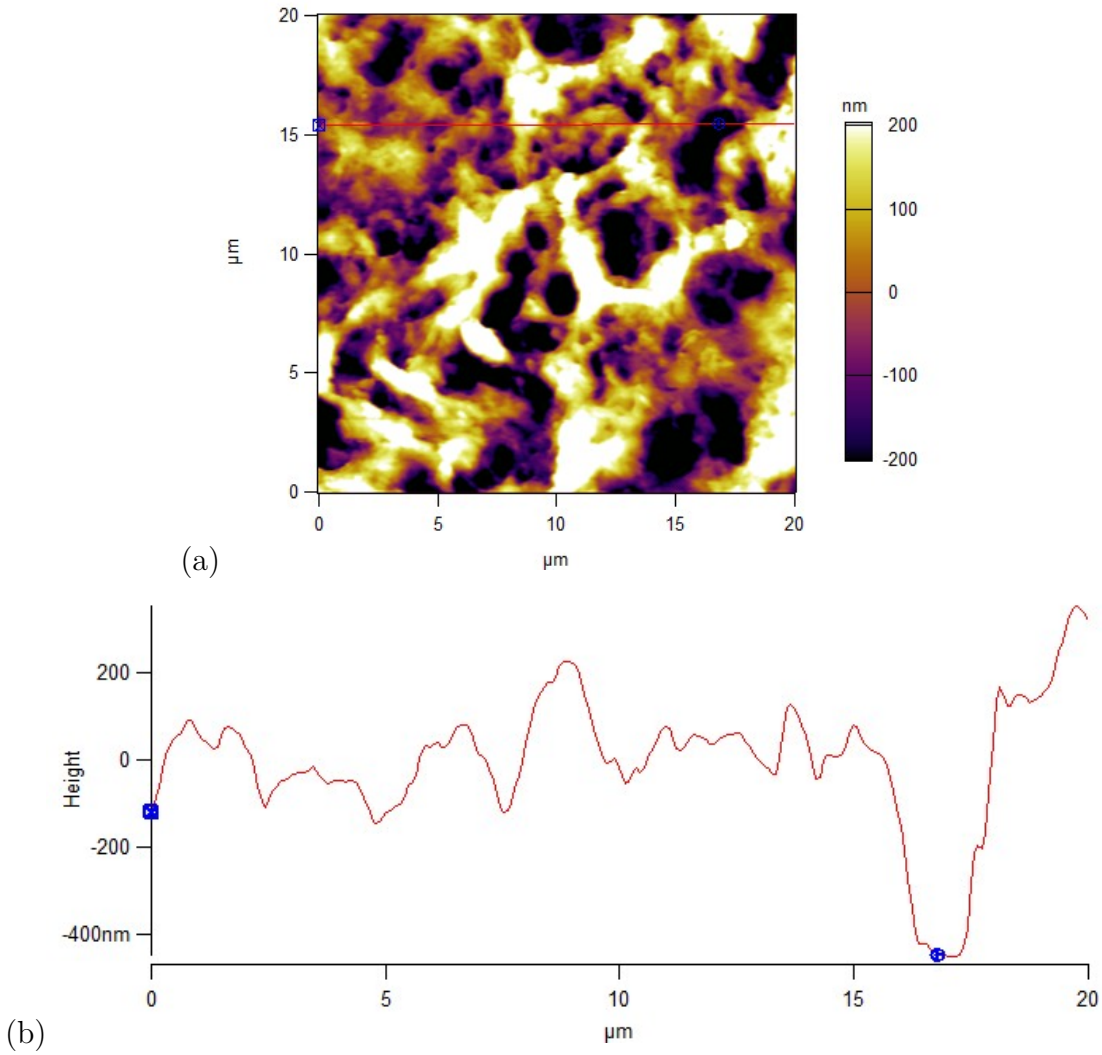

Figure 2.7: (a) 20 × 20 μm AFM topography image of the retinal blood vessels obtained from mouse eye, and (b) illustrates the cross section profile of the above topographic image showing the depth of the pore.

MSc student in the Merschrod group, Lucas D. Stewart [82], who mapped both the topography information and mechanical properties of the vascular regions.

The successful finding of identifying most of the microstructural features of the mouse eye advances the objective of this research, which is mapping the mechanical properties of retinal tissue. This finding also leads to many questions regarding eye, which will be discussed in more details in the future works section of the Conclusions chapter. ’

Chapter 3

Retinal tissue imaging and mechanical property mapping

3.1 Motivation

As mentioned in the previous chapters, diseases due to the degeneration of the retina result in the death of the photoreceptor cells (rod and cone) and the retinal ganglion cells (RGCs) which result in blindness. Loss of sight is treated using gene therapy or drug therapy. However, in the case of complete loss of the photoreceptor cells, gene or drug therapy is not effective [33]. As such, an alternative method of treatment such as tissue replacement is required. Nevertheless, the mechanical properties of the appropriate tissue should first be understood in order to use the best biomaterials to design the tissue [64]. For instance, the understanding of the retina as a highly active tissue with cells that are mechanically active and very sensitive provides vital information on retinal physiology and pathology that allows the designing of the appropriate tissue [47]. Based on this, both the morphological and mechanical properties of retinal tissue were mapped.

3.2 Experiment

3.2.1 Imaging in air

All topographic images in air of the retina were obtained through contact mode AFM. Silicon cantilevers coated with gold and chromium were used with a spring constant of 0.1 N/m to 0.3 N/m purchased from μmasch (HQ:CSC37/Cr-Au). The exact spring constant of the individual tip can be determined by the thermal calibration [81]. The scan size of each retinal image was 20 $\times$ 20 μm with a resolution of 256 $\times$ 256 pixels unless otherwise mentioned, and the scan rate was 1.0 Hz, which is the ideal scan speed for a small region using contact mode.

To map the retinal tissue, microstructural topographies were obtained from the inner layer (inner limiting membrane) through to the outer layer (retinal pigment epithelium) of the retina as Figure 1.12 indicates. Three different trajectories were taken along the retinal tissue in order to identify any artifacts as we were going along the tissue.

3.2.2 Determination of Young's modulus in air

Force curves were collected using the same instrument used for the imaging, which is MFP-3D atomic force microscope (Asylum Research). Also, force maps, which are, in brief, regular force curves taken at discrete points across a region of interest, were obtained. A gold–chromium coated AFM tip was used with a spring constant of 0.1 N/m to 0.4 N/m and resonant frequency close to 18 kHz. Initially, a 20 $\times$ 20 μm topographic image was taken of the area of interest with a scan speed of 0.5 Hz.

The sensitivity (invOLS) and the spring constant of each cantilever were determined for accurate measurements of the Young's moduli. The sensitivity was measured as the slope of the force curve obtained from a regular indentation of a hard

surface such as silicon wafer or mica. The Poisson ratio of the retina has been calculated in a previous paper to be 0.47 [83].

The apparent Young's modulus was taken from two different sections: the dry section and the fresh one. On each sample, 20 random force curves were collected for each 20 $\times$ 20 μm scan size. At these conditions, force curves were taken using the minimum indentation. Also, force maps of the sample were obtained at a resolution of 16 $\times$ 16, and 32 $\times$ 32 pixels, and each pixel represents a unique force curve. These force curves and maps were obtained with a velocity of 20 μm/s and trigger point of 5 nN. The JKR model, for accounting for adhesion force as previously described in Chapter 1, was used to evaluate retinal tissue elasticity from force-indentation measurements. To characterize the mechanical properties of retinal tissue, the average Young's modulus of the entire tissue was calculated using an automatic procedure that was created by Garrett McDougall, an undergraduate student in the Merschrod group. [84] Statistical analysis (a single-factor ANOVA test) was used in order to determine the significance of differentiation between retinal layers [83].

3.2.3 Imaging under fluid

To image in water, an initial scan of the area of interest was captured using AFM contact mode or tapping mode as described in Section 3.2.1. If tapping mode was used to scan the sample surface, tuning the tip in air is an additional step that is required and all the parameters will be saved for either mode. Experiments were performed using silicon cantilevers coated with gold-chromium with a spring constant of 0.1 N/m to 0.3 N/m and resonant frequency close to 18 kHz. The individual spring constant and resonant frequency of each cantilever calculated through thermal calibration [81].

After obtaining a topographic image in air, a micropipette was used to inject 10-50 μL water between the cantilever tip and sample. The AFM head was raised by 1 to

2 μm to allow space for the micropipette; otherwise, the tip will be damaged. Both the tip and sample are immersed in water, thereby a stiff cantilever is not required as the capillary force is eliminated and contact mode tips also work under liquid perfectly for tapping mode. The cantilever oscillation was tuned to a frequency of 7-9 kHz, and the drive amplitude was fixed to be around 1 V. The force was adjusted by minimizing the amplitude set point while the sample surface was scanned. Retuning of the cantilever tip should be done for tapping mode, which is used to protect the sample from damage.

Topographic images, 20 $\times$ 20 μm, with resolution of 256 $\times$ 256 pixels were obtained along the retina with a scan speed of 0.5 Hz. The retinal tissue was mapped under water following the trajectory that is indicated in Figure 1.12.

3.2.4 Determination of Young's Modulus under fluid

To perform force spectroscopy experiments under water, the same MFP-3D AFM and coated silicon cantilevers were used. Both the sensitivity (invOLS, which relates cantilever deflection to photodetector voltage and measured in nm/V) and the spring constant of the cantilever were acquired through the thermal calibration [81]. A 20 $\times$ 20 μm topographic image of the area was obtained with scan rate of 0.5 Hz.

In order to map the Young's modulus of the retina, we switched to contact mode after imaging in water using tapping mode. For each retinal layer, 20 random force-distance curves, 16 $\times$ 16 pixels, and 32 $\times$ 32 pixels were recorded. Both force curves and force maps were performed in fluid with a tip velocity of 20 μm/s and trigger point of 5-10 nN.

3.2.5 Histology of the frozen section

To correlate with the atomic force microscopy maps, the specimens were stained in a histological manner at the completion of atomic force microscopy measurements. An interval of 20.0 minutes in 4.0% hematoxylin and paraformaldehyde marking was performed as explained in references 85 and 80. Snaps of the marked histological specimens were taken using Leica DM4000.0B light microscopes with Q mounted imaging camera and Open Lab software. All the specimens used met the protocols set by Memorial University's Institution of Animal Care Committees and supervised by Drs. Driedzic, Paradis, and Gendron.

3.3 Result and discussion

3.3.1 Dry tissue images and Young's modulus measurements

Retinal tissue was mapped using atomic force microscopy in order to obtain high-resolution images of the topography. Figure 3.1 presents height images of retinal tissue layers obtained in air by contact mode. As is mentioned in the previous chapter, the colour scale bar represents the height of the features: the darker the color, the lower the features and conversely. Retinal layers were mapped from the inner layer to the outer layer and these layers are identified in Figure 3.1.

In order to determine the mechanical properties of retinal tissue, force maps were performed along the retinal layers. The force mapping experiments are required to take individual force curves at discrete points. Therefore, to map the retinal tissue, force mapping was obtained for each 20×20 μm scan and the average Young's modulus was determined. The minimal indentation JKR model was used to determine the Young's modulus.

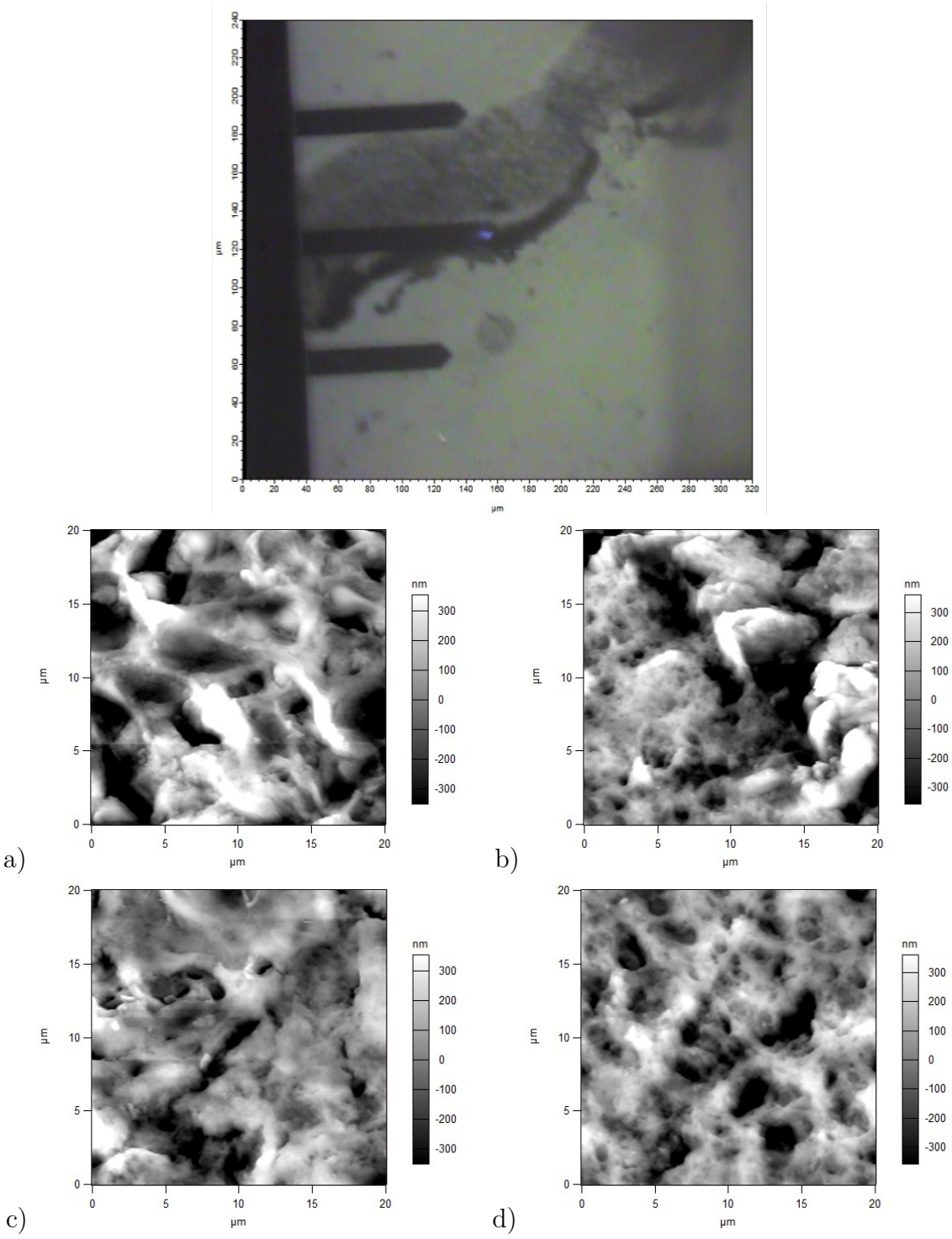

Figure 3.1: AFM camera capture of the dry tissue (top). Height images of various layers of the retina starting from the inner to the outer layer (bottom) representing (a) retinal ganglion cells, (b) bipolar cell,(c) retinal photoreceptors, and (d) retinal blood vessels.

Initially, 16 × 16 pixel resolution force maps were acquired for each 20 × 20 μm scan. The average Young's modulus for each force map in Figure 3.2 are presented in Table 3.1. An ANOVA test was done to test the difference between each layer. However, due to the complexity of the tissue, the differences between layers were not all statistically significant. Therefore, more data points were then collected.

Table 3.1: Average Young's modulus was obtained by the minimal indentation JKR model at a resolution of 16 × 16 pixels of retinal layers and their standard deviations analyzed.

	Young's modulus (MPa) ± standard deviation (MPa)
Retinal ganglion cells	11 ± 4
Bipolar cell	10 ± 3
Retinal photoreceptors	07 ± 2
Retinal blood vessels	09 ± 2
Average value	11 ± 3

The retinal tissue consists of sensitive and mechanically active cells as is mentioned in section 1.3.1 [47]. Therefore, high resolution details about retinal tissue mechanics will be critical to understand certain features of the retina. Therefore, more discrete points were obtained in order to see the significance of differences between layers. Maps with a resolution of 32 × 32 pixels were performed in retinal layers that are shown in Figure 3.1. The average Young's modulus of each 20 μm scan is presented in Table 3.2. The difference between layers was analyzed (ANOVA test), and this test showed that there are differences between layers.

If both data from Tables 3.1 and 3.2 are compared, the Young's modulus values are different as more data points were accounted in a resolution of 32 pixels. However, the same trend is seen if the values are compared with the area. For example, the inner layers of the retina appear to be stiffer than the outer layers as their average

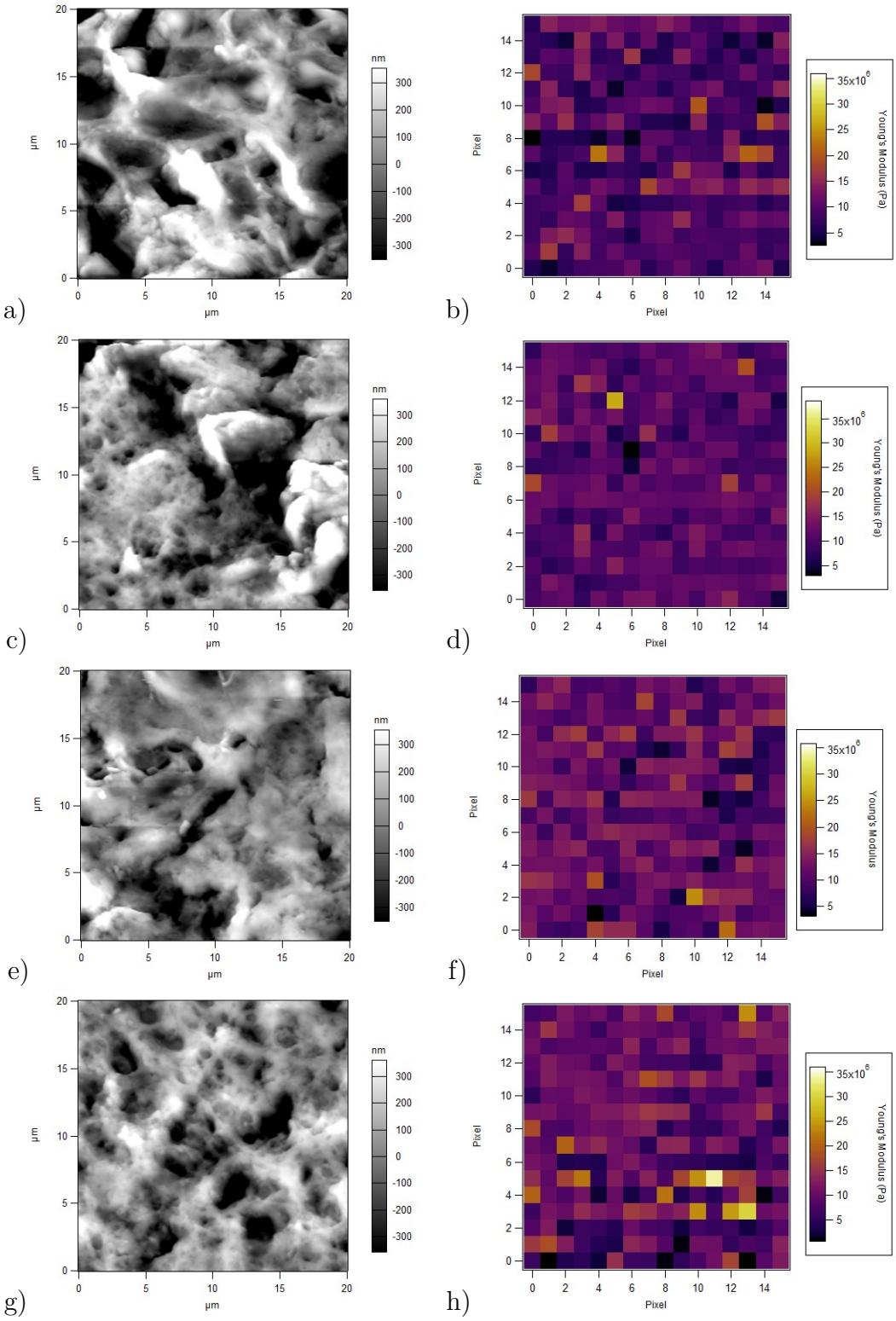

Figure 3.2: Height topographic images of dry retinal layers as they are identified earlier in Figure 3.1 (left), and their corresponding force maps (right).

Table 3.2: Average Young's modulus was obtained at a resolution of 32 × 32 pixels of retinal layers and their standard deviation analyzed by the minimal indentation JKR model.

	Young's modulus (MPa) ± standard deviation (MPa)
Retinal ganglion cells	91 ± 15
Bipolar cell	83 ± 13
Retinal photoreceptors	68 ± 12
Retinal blood vessels	56 ± 13
Average value	78 ± 14

Young's moduli are larger.

Since the retina layers were mapped, the average Young's modulus value of the retina was determined. By joining force maps together (through an automatic procedure that was also created by Garrett McDougall [84], to combine more than two force maps, the average Young's modulus of the whole retina was determined to be 78 ± 14 MPa. The average Young's modulus value of each column from the joined map was also calculated and plotted with the distance along the retina, starting from the inner layer toward the outer layer, as shown in Figure 3.3. In fact, the scratched image in Figure 3.3, taken by optical microscope, is the same sample slide used to map the mechanical properties of the retina. This scratch feature helped us to make correlations between AFM results and optical microscope image.

Our analyzed data provide a complete mapping of the mechanical properties of retinal tissue from the inner to the outer layers. Using atomic force microscopy and force spectroscopy, we determined the apparent Young's modulus of the retina to be 78.02 ± 14.32 MPa. The Young's modulus value was determined at relatively small scale. However, due to the complexity of the tissue more data are required.

The stiffness of the tissue varies along the retina. Therefore, we made an assump-

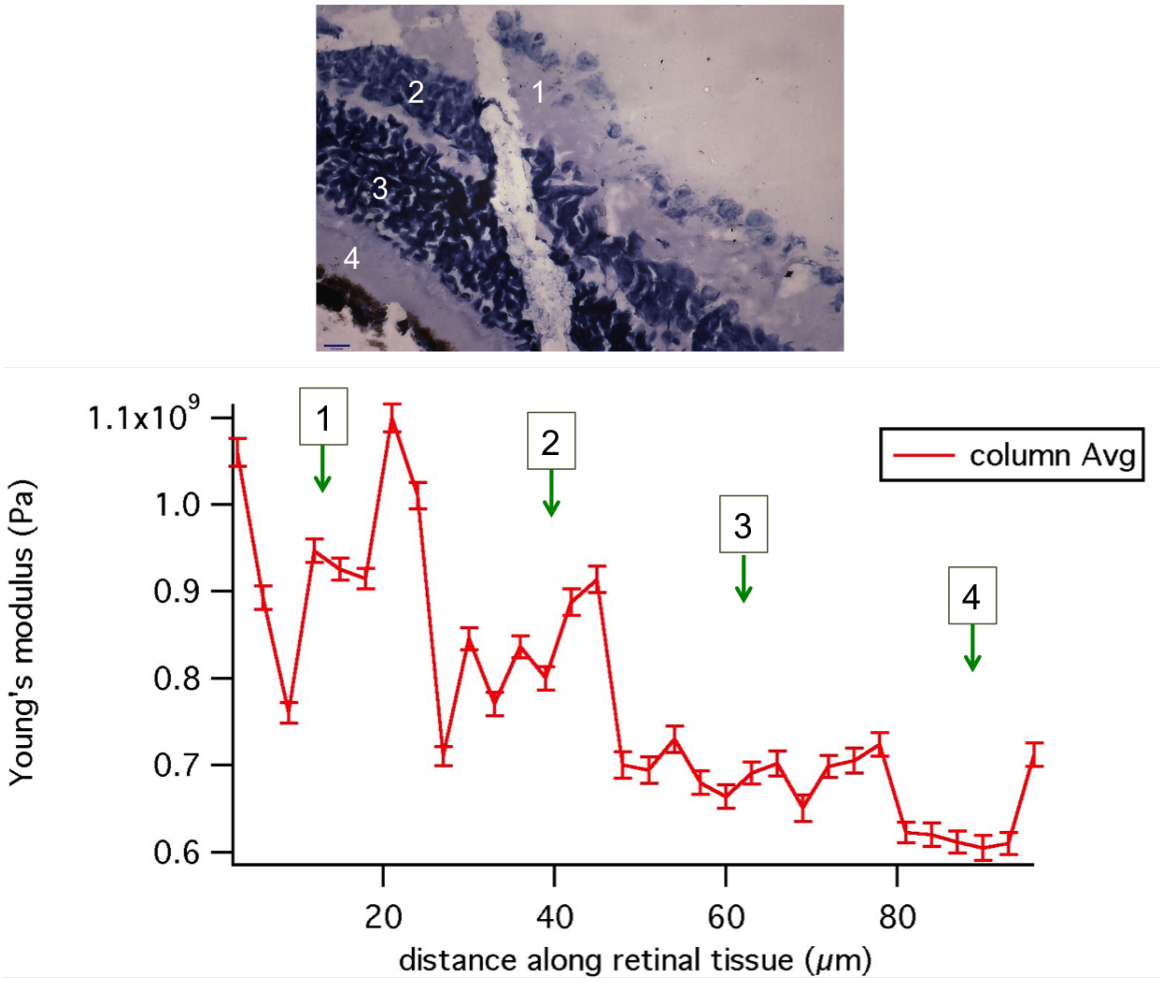

Figure 3.3: An optical microscopic image of a transverse section of the whole retinal tissue showing the scratch along the tissue (top). The plot displays the average Young's modulus value (Pa) as a function of distance along the retina (bottom).

tion in order to correlate the region that was mapped by the AFM with the optical microscope. This assumption states that each 20 $\times$ 20 μm scan represents a unique layer in the retina. Although there is some overlap between layers as some of the retinal layers are either less or greater than 20 μm, the aim in this thesis is to measure the average Young's modulus of the whole retinal tissue. Thus, this assumption is a good starting point in this case. We would introduce bias by choosing which section of the image to average and define as a layer. In the discussion below we present a means to identify different regions more exactly by joining together adjacent images.

The Young's modulus of the inner layers was approximately 100 MPa whereas the Young's modulus of the outer layers was 50 MPa. Figure 3.3 shows how the Young's modulus decreased in moving to the outer layers, which means that the inner layers tend to be stiffer than the outer layers. Although this difference does not appear to be large, we can conclude that the inner layers have association with neuronal functioning. The retinal neuron layers, as mentioned in Section 1.3.1, consist of neuronal cell types that lead to stiffening of the tissue. Thus, this increases in the Young's modulus values of the inner layers are due to the density of the neuronal cell, including the ganglion cell and bipolar cell. The increase in the Young's modulus of the inner layers was assumed to be associated to the neuronal cells functioning as these layers mostly consist of different neuronal cell types. Therefore, the reduction in the Young's modulus of the outer layers can be correlated to the photoreceptors and the retinal pigment epithelium (RPE) functioning. The outer layers mostly consist of photoreceptor cells (rods and cones), blood vessels, membrane, and collagenous zone. This explains the decrease in the Young's modulus values of that layer.

3.3.2 Hydrated tissue images and Young's modulus measurements

Most previous literature that focuses on studying the mechanical properties of biological materials using atomic force microscopy reported results for hydrated samples [86–88]. However, our results in the previous chapter were obtained from dry samples. Furthermore, measuring the mechanical properties of dry sample is usually considered to be an issue for biological samples as drying is different than their native environments. Thus, this may lead to variations on the morphological and mechanical properties of the sample. In fact, previous studies showed that the Young's modulus value in aqueous medium is two to three orders of magnitude lower than that measured at ambient conditions [89–91]. In order to observe this difference, both the topography and the Young's modulus of the tissue were mapped under fluid using the same instrument.

Similar areas were imaged under fluid using tapping mode and these images are illustrated in Figure 3.4. These images are not exactly from the same spot, but they are taken from the same area as the previous images. The images are presented here to show differences between images obtained in air and in fluid. Variation between images in Figure 3.1 and Figure 3.4 is that features more swollen in fluid more than in air. This swelling appears through higher features and wider pores.

The Young's modulus of hydrated tissue was mapped for each 20 $\times$ 20 μm scan. This time, the Hertz model summarized in section 1.2.1.1 was used to determine the Young's modulus of the tissue. A different model was used to obtain the Young's modulus of hydrated tissue than the model used for the dry one because the tip-sample adhesion force and the jump to contact, the action of the tip that appear during the approach phase, are insignificant in fluid. Thus, the minimal indentation

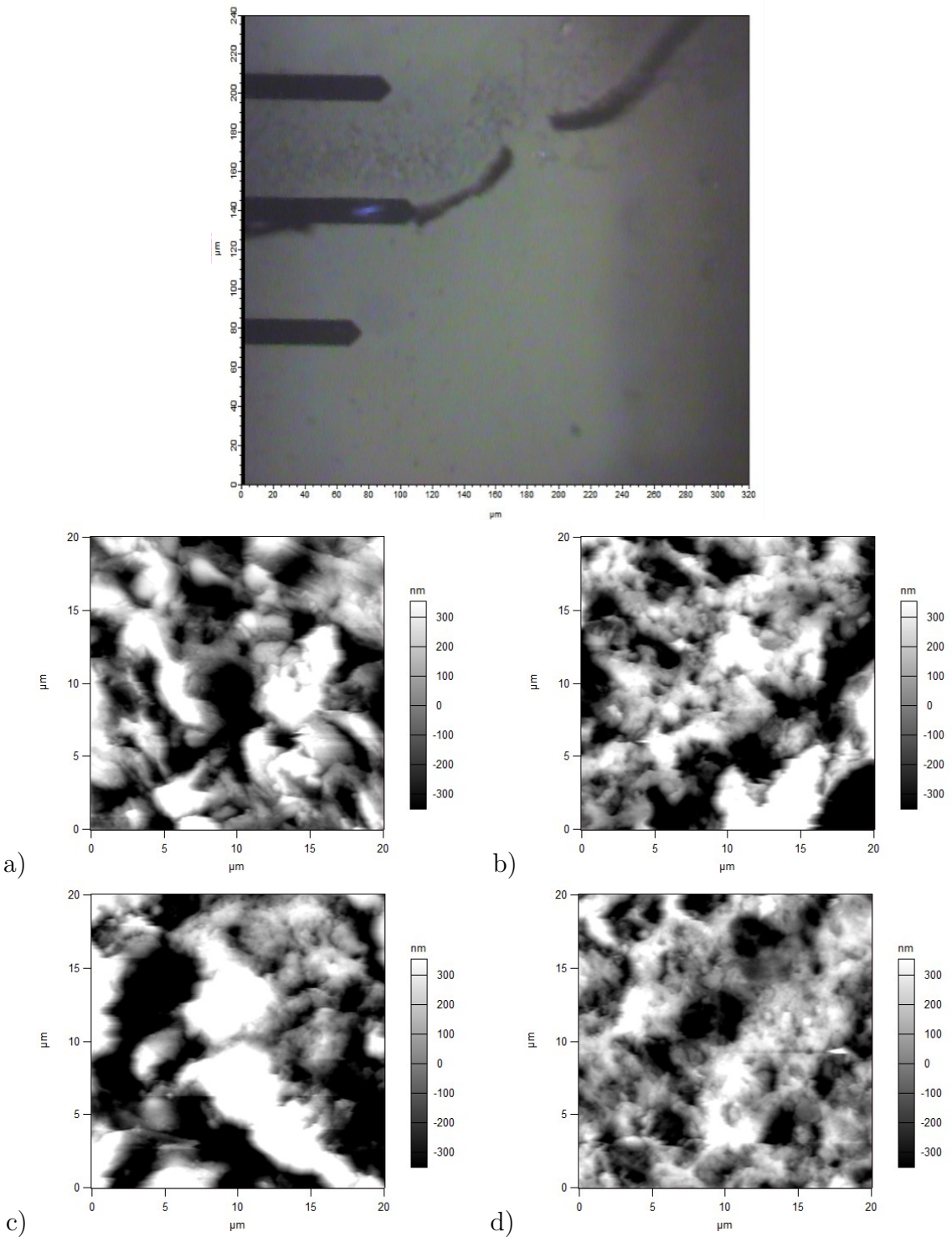

Figure 3.4: AFM camera capture of the hydrated tissue (top). Height images of various layers of the retina starting from the inner to the outer layer (bottom) representing (a) retinal ganglion cells, (b) bipolar cell,(c) retinal photoreceptors, and (d) retinal blood vessels.

JKR model is not suitable to be used for the determination of the Young's modulus in fluid, and the Hertz model is used instead.

Force mapping of the retinal tissue was performed following the same trajectory of the topographic imaging of dry tissue, moving from the inner layer to the outer layer. For each 20 × 20 μm scan, a force map was obtained at a resolution of 16 × 16 pixels. The average Young's moduli of each force map shown in Figure 3.5 are presented in Table 3.3. A statistical test was performed to test the variations between layers.

Table 3.3: Average Young's modulus values at a resolution of 16 × 16 pixels of hydrated retinal layers and their standard deviation analyzed by the Hertz model.

	Young's modulus (MPa) ± standard deviation (MPa)
Retinal ganglion cells	5 ± 1
Bipolar cell	4 ± 1
Retinal photoreceptors	2 ± 1
Retinal blood vessels	2 ± 1
Average value	3 ± 1

For the same reason mentioned earlier about the complexity of retinal tissue, more discrete points are required. When the Young's modulus values at a resolution of 16 × 16 pixels are compared for both air and fluid (see Tables 3.1 and 3.3), we can not see significant differences between the average values. Therefore, a 32 × 32 pixels force map was performed for each 20 × 20 μm scan. The average Young's modulus was calculated and values are presented in Table 3.4. An ANOVA test of the differences between retinal layers in the hydrated samples with the higher resolution data showed statistically significant differences.

Averaging the Young's modulus value of joined force map, the apparent Young's modulus of the hydrated tissue was determined and compared with the apparent Young's modulus in air in Table 3.5. Additionally, column averaged values were

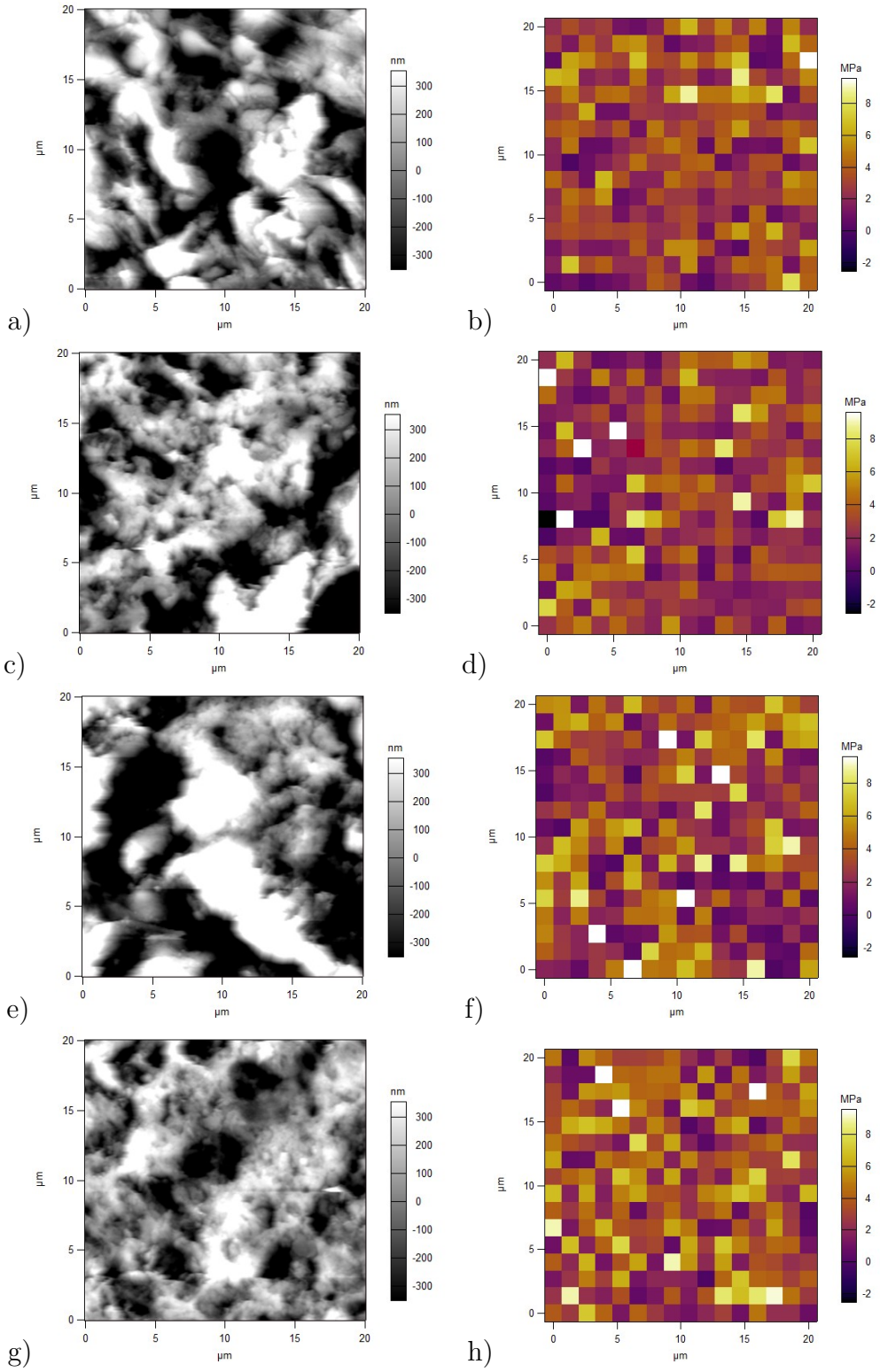

Figure 3.5: Height topographic images of hydrated retinal layers, are identified in Figure 3.4 (left), and their corresponding force maps (right).

Table 3.4: Average Young's modulus values at a resolution of 32 × 32 pixels of hydrated retinal layers and their standard deviation analyzed by the Hertz model.

	Young's modulus (MPa) ± standard deviation (MPa)
Retinal ganglion cells	0.854 ± 0.179
Bipolar cell	0.909 ± 0.205
Retinal photoreceptors	0.618 ± 0.181
Retinal blood vessels	0.698 ± 0.165
Average value	0.744 ± 0.313

plotted as a function of distance along retinal tissue and presented in Figure 3.6.

Table 3.5: Average Young's modulus of retinal tissue for both dry and hydrated tissue and their standard deviation analyzed by the minimal indentation JKR model and Hertz model respectively.

	Young's modulus (MPa) ± standard deviation (MPa)	statistical difference
Dry tissue	78.02 ± 14.32	Yes
Hydrated tissue	0.744 ± 0.313	

The results that were obtained from hydrated tissue showed similar result to that obtained at ambient conditions. The Young's modulus value decreases as a function of distance, as seen in Figure 3.6. Although that some region appears to be either stiffer or softer than that in air, we can not definitely scan the exact regions without an overlap. However, the Young's modulus value of the inner layers is still larger than that of the outer layers. Therefore, the increase in the Young's modulus means stiffening of the inner layer while the decrease in the Young's modulus means softening of the outer layer.

The average Young's modulus in aqueous environment was determined to be 0.744 ± 0.313 while at ambient conditions it was 78.02 ± 14.32. This is a statistically

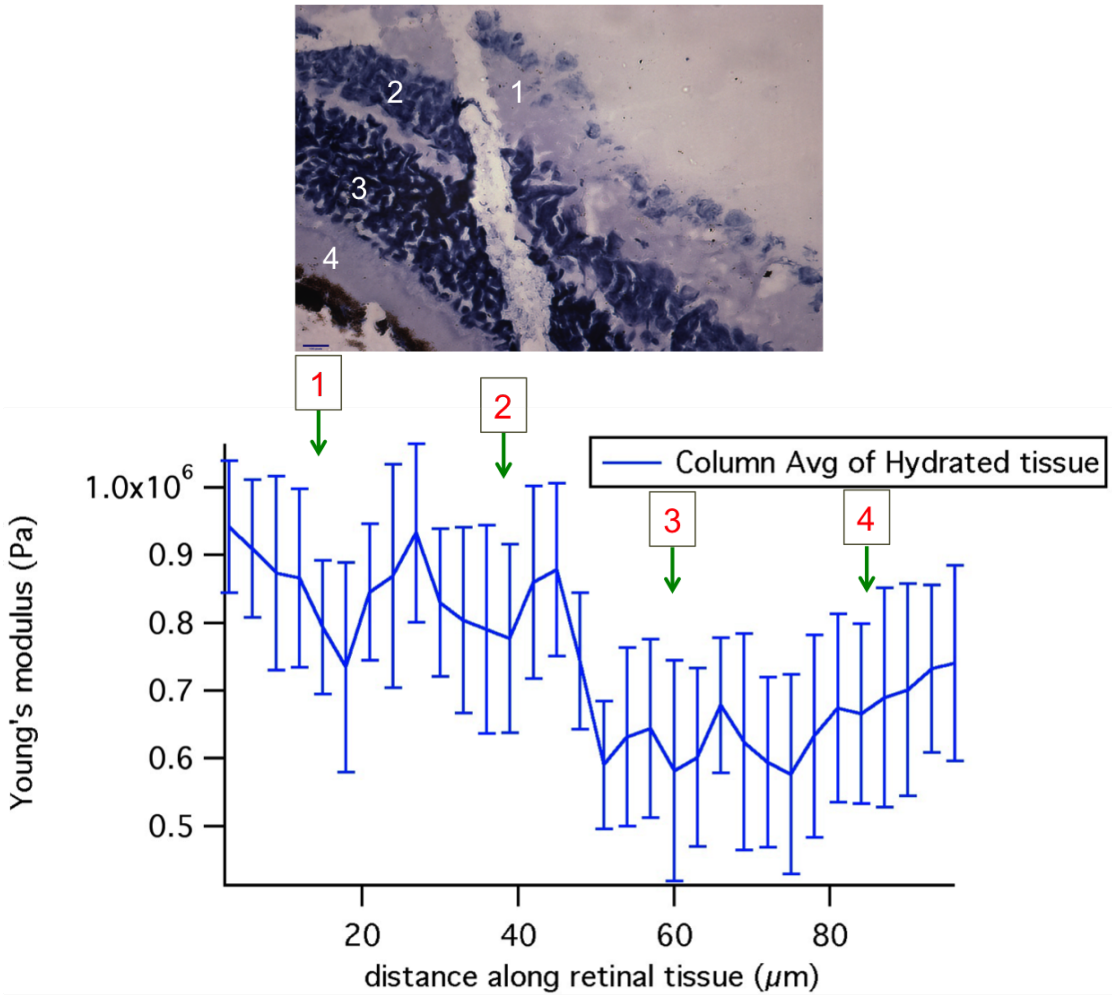

Figure 3.6: An optical microscopic image of a transverse section of retinal tissue showing the scratch along the tissue (top). The diagram displays the average Young's modulus values (Pa) for hydrated tissue as a function of distance along the retina (bottom).

significant difference ($P = 1.54954 \times 10^{-77}$ from the Welch test), and the details of the statistical analyses are provided in Appendix C. By comparing the apparent Young's modulus of the retina in both conditions, we can see that the Young's modulus value in fluid decreases by around three orders of magnitude compared with that in air. This reduction was studied in previous papers which explained the reasons behind the decrease in the Young's modulus value. One of these reasons is that water bridges formed between peptide chains when the collagen fibers is studied [92]. Another reason can be attributed to the formation of water bridges between lipid molecules in membranes [93]. Since the retina tissue is mixture of collagen fibers and membranes, these two reasons can be applied for our case.

3.4 Conclusion

The mechanical properties of retinal tissue were determined using atomic force microscopy. The apparent Young's modulus was found to be different from one region to the other. The differences between each layer of the retina was tested using an ANOVA test. Although this difference was not sufficient for our purpose as the ANOVA test does not show significant variations between layers, it still leads to the importance of measuring the Young's modulus for smaller scan sizes. The average Young's modulus of the retina was determined to be 78.02 $\pm$ 14.32 MPa. Our measurements showed that the inner layers appear to be stiffer than the outer layer. While the variations between the inner and the outer layers do not tend to be large, we have explained these differences based on their functions. The increase in the Young's modulus of the inner layers can be attributed to the density of neuronal cells. On the other hand, the reduction in the Young's modulus of the outer layers can be attributed to the photoreceptor cells, the retinal pigment epithelium (RPE), and blood vessels

functions.

The effect of hydration on retinal tissue was also studied by AFM. The apparent Young's modulus of the retina was determined to be 0.744 ± 0.313 MPa, which is lower than that in air (78.02 ± 14.32 MPa). The average Young's moduli for both dry and hydrated sample were statistically different. Hydration effects from previous studies were found to decrease the Young's modulus by two to three orders of magnitude and this what was concluded in this thesis as well. This reduction in the Young's modulus in aqueous environment was examined for other types of biological samples in previous studies and explained by the formation of water bridges [90, 92].

Although the Young's modulus values are different in ambient conditions than in aqueous environment, the same trend from the inner layers to the outer layers is seen. The inner layers have a larger Young's modulus than the outer layers; thus, the inner layers appear to be stiffer than the outer layers. The differences along the retinal tissue do not appear large, but we assume that this has implications of cells functioning.

Chapter 4

Conclusions and future work

4.1 Conclusions

Our data provide an insight into the structure of the eye on the nanoscale using a powerful tool, Atomic Force Microscopy (AFM), for better understanding of the structure beyond the optical microscope. This thesis presents the first complete AFM mapping of the morphology of the rainbow smelt (*Osmerus mordax*) and mouse (*Mus musculus*) eyes. This first step toward mapping the whole eye has led to many interesting questions. Only a few of them are accomplished in this thesis and that of a collaborator, Lucas D. Stewart, whereas there are more questions to investigate in future.

This thesis also studied the morphological and mechanical properties of retinal tissue of mouse *Mus musculus*) eye using atomic force microscopy. The retina was mapped from the inner to the outer layer. The average Young's modulus at ambient conditions, analyzed by the minimal indentation JKR model, was calculated for each 20×20 μm scan. Joining force maps obtained at a resolution of 32×32 pixels, the average Young's modulus of the retina was determined. Furthermore, through

averaging each column of the joined maps and plotting the Young's modulus as a function of distance along the retina, the complexity of the tissue was seen. The stiffening of the layers was varied along the retina depending on their functions. There was an increase on the Young's modulus of the inner layers and decrease on the Young's modulus of the outer layers. While the inner layers contain different neuronal cell types, the outer layers consist of membrane, blood vessels, and collagenous zone. This tends to stiffen the inner layers of the retina more than the outer layers. This finding is under development through collecting more discrete points and scanning in more detailed scales, as will be mentioned below in the future works section.

The effect of hydration on the retinal tissue was also examined by atomic force microscopy. The hydration of the retinal tissue showed swelling in the morphology as some features appear higher, and pores wider. Hydration has also a significant effect on the Young's modulus of the retina. The apparent Young's modulus value decreased by two orders of magnitude in fluid compared to that under ambient conditions. This reduction in the Young's modulus is because of the formation of water bridges within tissue which lower the Young's modulus relative to that in air. While the apparent Young's modulus is different in air than that in fluid, we still have the same conclusion from mapping the Young's modulus of dry tissue. The Young's modulus of the inner layers is larger than the Young's modulus of the outer layers. Thus, inner retina is stiffer than outer retina.

4.2 Future work

This successful mapping of the morphological eye information and mechanical properties of retinal layers build the foundation of future research investigations. Thus, more questions regarding our work are accounted for in order to have a clear results

and understanding for our finding in this thesis.

Having a complete mapping of the normal eye advances the investigation of the differences between normal and diseased eyes as the normal eye has not been well studied at the nanoscale before. Therefore, a complete mapping, starting from the cornea toward the optic nerve, of diseased eye is an important step for comparing the morphology of normal eye and diseased one to realize the variation on the same scale.

Before we move to in-depth future works on the mechanical properties of the retinal tissue, extracting the tissue is essential for more accurate results. As the tissue is extracted, a complete mapping of the mechanical properties are required at a smaller scale than that we have in this thesis to understand the tissue's mechanical properties in more detail. For our current result, we made an assumption that each 20 μm scan represents a unique layer in the retina, and this was an acceptable assumption to start with. However, for more accurate results, the thickness of each layer should be measured by optical microscope and correlated with the AFM measurements. As mentioned in section 1.3.1.1, most diseases that affect retina are a type of degeneration. It would be important to see the differences in morphological and mechanical properties between the normal and diseased eye.

Determining the elastic response of retinal tissue leads to the importance of the determination of viscoelastic effects as well. Up to now, the retinal tissue has been treated as an elastic tissue that produces an elastic deformation instantly with negligible time delay. In fact, soft tissues like eye tissue show a significant time dependent deformation. To explore this possibility, the viscosity is considered to be measured by AFM through creep measurements. Creep measurement is time dependent deformation that shows mechanical response over time. This can be seen when a constant load is applied and the indenter keeps sinking into the sample until a creep curve is generated, which is the indentation depth with time [94]. By fitting the creep curve to

one of three models an access to the viscosity of the material is given. These models are the standard linear solid, Burgers model, and a two-dashpot Kelvin model [95]. In our case, the Burgers model should be used as it has been found that this model is used to describe creep behaviour for biomaterials.

Appendix A

Force scanning

A.1 Introduction

Since the 1990s, atomic force microscopy studies have applied force mapping to provide nanoscale topographical and mechanical details concerning the substrate. Force mapping encompasses individual force generation curves at discrete points on the material, which facilitates height and stiffness values 7.0, 6.0 calculations [96,97]. Such a workhorse model is straightforward and less complex than force mapping, which makes the implementation process easy with various atomic force microscopies. However, the technique is also observed as a slow formula involving less lateral resolutions, which is not ideal for various biological uses. Therefore, a novel energy-scanning model using atomic force microscopy is used to capture high resolutions topographical images of soft biological substances while quantifying their mechanical features [97].

Force scanning is lauded as a straightforward model applicable to various substances and testing environment, and it does not require modification to standard atomic force microscopy [97]. The execution of the force scanning model is simple and widely applicable to any deformable substance, from cartilage to agarose gels

to living cells. The force-scanning model requires no special equipment, cantilevers, or standardization to atomic force microscopy technologies. Force scanning viability depends on the clear contact-mode images. Notably, acquiring contact-mode image facilitate the production of spatial modulus maps [97]. Figure A.1 explains simply how the force scanning works where the maximum apply force and number of scans depend on the material that is tested. For force scanning, multiple contact-mode images were required in order to obtain the corresponding force-distance curves, which can provide high-resolution imaging with matched modulus maps [97].

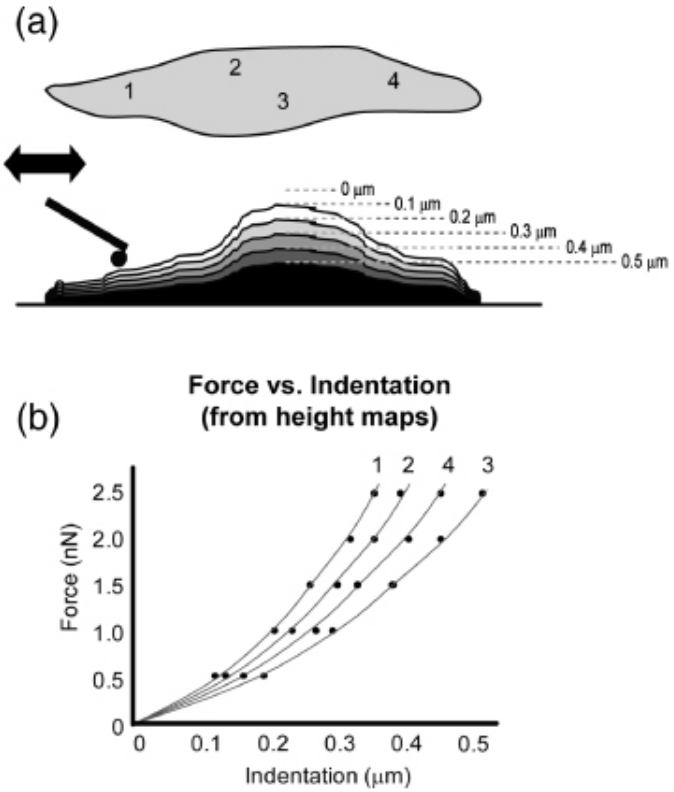

Figure A.1: (a) Force scanning technique requires a multiple contact-mode scans with increasing set points (applied forces) depending on the material. Each topographical image corresponds to a force-distance curve, and these force curves (b) were used to calculate the Young's modulus at each point. This technique easily provides a topographical image and its matched stiffness image which is very useful for biological sample in order to determine the mechanical properties quickly [97].

A.2 Stack image method

An MFP-3D atomic force microscopy was used for topographic imaging. Experiments were accomplished using silicon cantilevers coated with gold-chromium (HQ:CSC37/Cr-Au) with spring constant of 0.1 N/m to 0.3 N/m and resonant frequency near to 18 kHz. The exact spring constant and resonant frequency of the individual cantilevers were determined using the thermal calibration [81].

Initially, a topographical image was captured though simple contact mode AFM imaging producing a definite topographical map. Then, the cantilever tip penetrated into the sample through applying a downward force (until the deflection set point was reached) in order to obtain a regular force curve. Multiple scans were taken with increasing set point (starting from 0 V to 1.0 V). Six scans were obtained per sample. Depending on the sample material, both the maximum force and number of scans may differ. I used an automated procedure, developed by Ryan Wilkins, an undergraduate student in the Merschrod Group, to superimpose the six scans and relate the different forces to the height.

This procedure works by fitting each force-distance curve to the minimal indentation JKR model, and calculating the Young's modulus as is shown in Figure A.2. The value of the Young's modulus corresponds to the topographical point. The Poisson's ratio ν of retinal tissue was assumed to be $\nu = 0.4$ as it is mentioned earlier [83]. The force-distance curve was collected using the same parameter that was previously used in order to map the Young's modulus of the retina. Force curves were obtained by indenting the AFM tip into the sample at a velocity of 20 μm/s and trigger point of 5 nN.

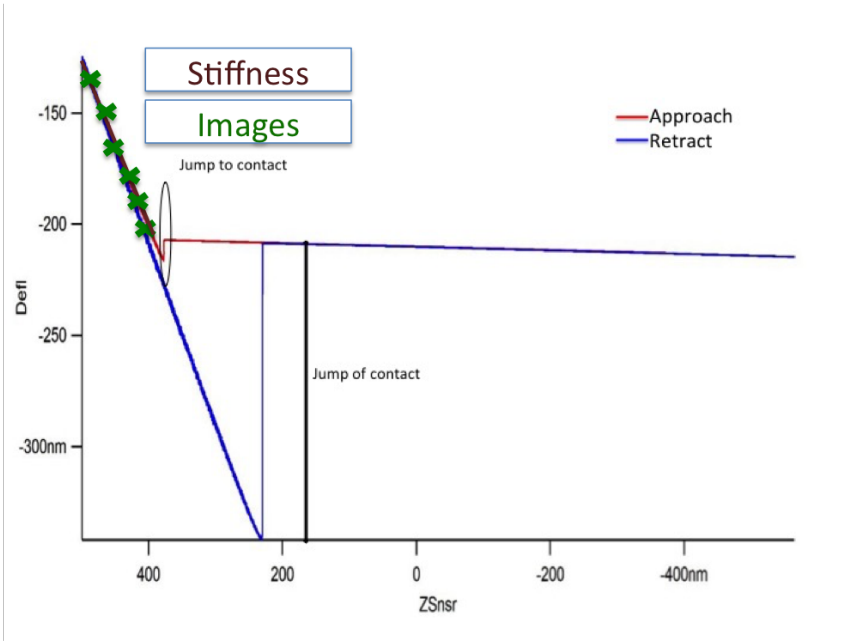

Figure A.2: Force curve diagram showing the fitting line of the minimal indentation JKR model in order to obtain a stiffness map.

A.3 Results and discussion

Force scanning on the mouse eye were obtained along the retina and the choroid, which provides a fair topographical images with spatially matched stiffness map. Figure A.3 illustrates both the height topographical images and stack images (stiffness map) of the retinal tissue and the choriocapillaris. From the image stack, the stiffness of the sample can be measured qualitatively as the color bar shows in Figure A.3. These stiffness maps show the complexity of the retina and the choroid as both tissues consists of multilayer. Therefore, this technique is very useful for biological tissue as it measures quickly the mechanical properties.

Comparing the overall results from the force mapping and force scanning, we can see that both methods lead to similar results. Force scanning determines the stiffness quantitatively whereas the force mapping determines the stiffness of the sample qualitatively. Therefore, initial knowledge about the sample can be obtained by performing

a quick force scanning method.

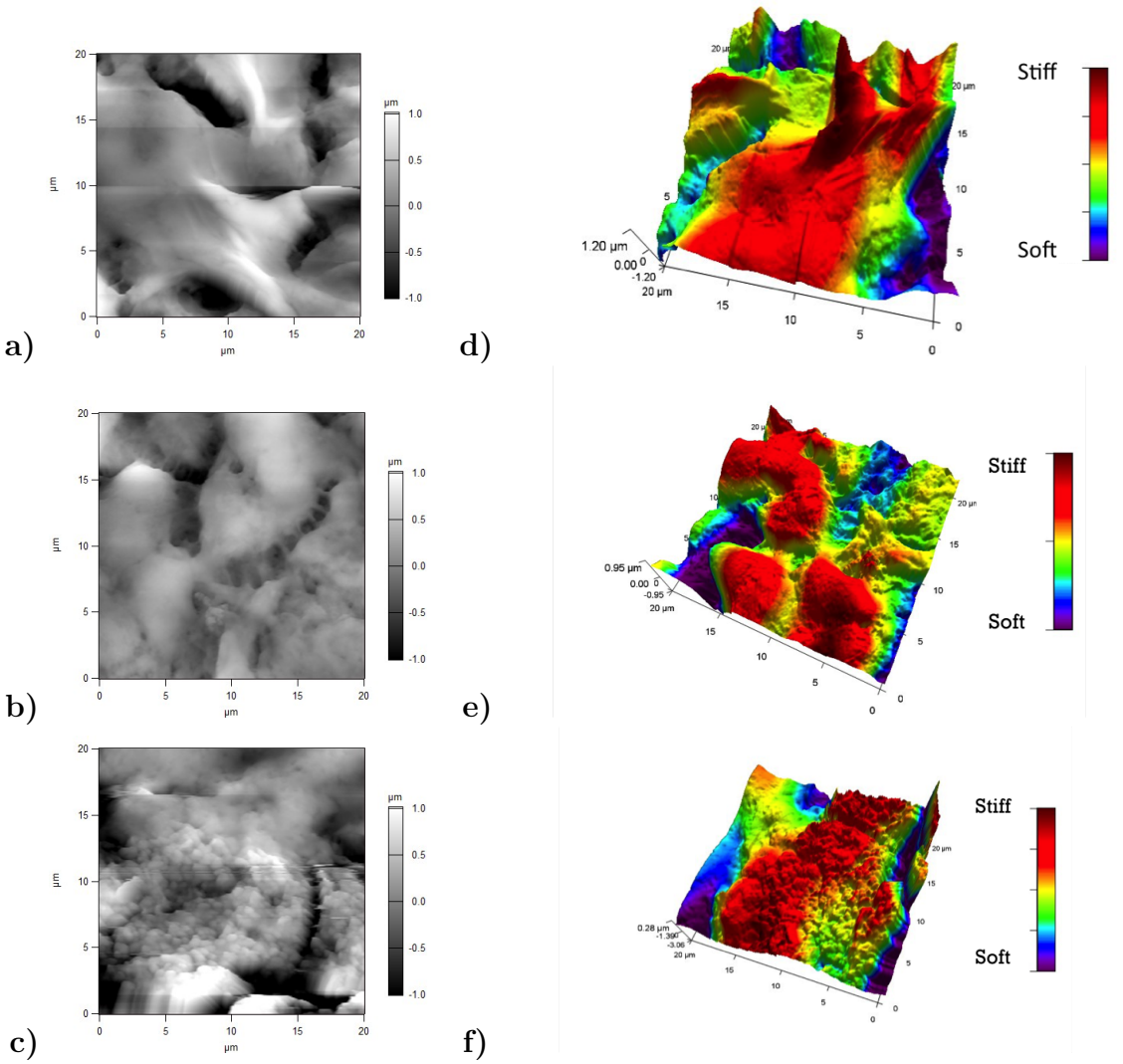

Figure A.3: The topographical height images of ganglion cells, photoreceptor cells, and the choroid are illustrated in a, b, and c respectively, and their corresponding stiffness maps d, e, and f, which was obtained from the force scanning technique. The color bar indicates the stiff area (red), and the softer area (purple)

A.4 Conclusion

Force scanning is useful technique for evaluating the mechanical properties of any sample that can be imaged by AFM. This novel method can rapidly provide a topographic image of the area of studies and matched stiffness map. Force scanning method is also applicable for soft and stiff samples that are imaged be AFM in air or fluid. When both force mapping and force scanning are compared, force scanning has the advantage of higher resolution in shorter time. All these advantages that are mentioned above lead to the importance to develop this method for the use of assessing other mechanical properties, including adhesion force [97], viscoelasticity.

Appendix B

Choroid

B.1 Motivation

The choroid is the eye vascular tissue that lies between the sclera and the Bruch's membrane as shown in the Figure 1.11 [44]. More than 70% of the blood flow to the eye goes to the choroid [98]. It has five layers starting from the one that in contact with the retina, which is Bruch's membrane, three vascular layers and suprachoroidea [99]. The tissue is very important in the eye because it is associated with choroidal inflammation and common retinochoroidal diseases including diabetic retinopathy, as well as age-related muscular degeneration [100]. Such sensitivity of the tissue implies that mapping of the tissue is an important step when addressing retinal diseases because the choroid attaches to the retina through the Bruch's membrane. As such, the high-resolution imaging and force mapping were obtained during the project.

B.2 Experiment

The topography of the choroid was obtained in air and under water through contact and tapping mode AFM imaging respectively, using MFP-3D atomic force microscopy.

Silicon cantilevers coated with gold-chromium (HQ:CSC37/Cr-Au) with spring constant of 0.3 N/m were used. Both the individual spring constant and the resonant frequency were determined by the thermal calibration method [81]. A 20 $\times$ 20 μm down to 5 $\times$ 5 μm topographic images with resolution of 256 $\times$ 256 pixels of the choroid were obtained with a scan rate of 1.0 Hz.

The Young's modulus was also calculated for both dry and hydrated tissue following the same procedure that was used to calculate the Young's modulus of the retina in both conditions.

B.3 Results and discussion

Both the topography and the mechanical properties of the choroid were mapped by AFM and force spectroscopy respectively in both dry and hydrated conditions. The topographic images in air and under fluid, presented in Figure B.1, show similar feature of the choroid; however, the height of the feature might vary. Figure B.2 presents a higher resolution image of the choroid, which shows clearly the structure of the choriocapillaris.

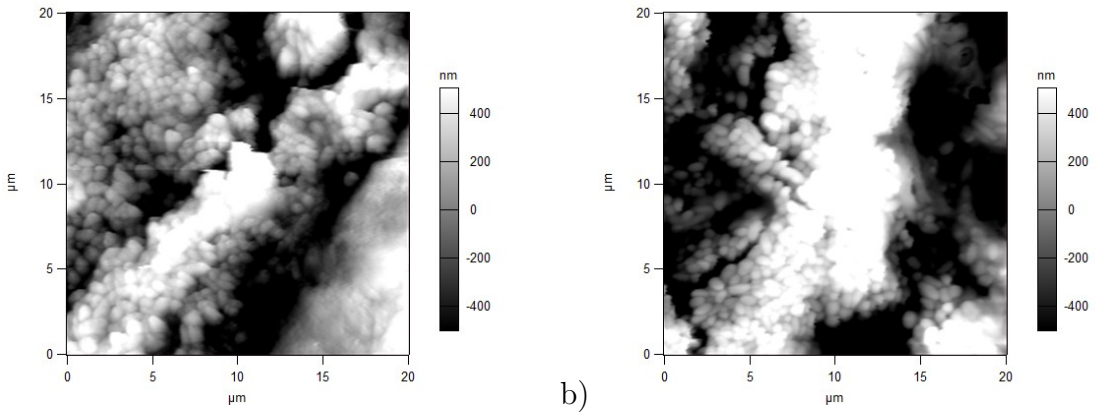

Figure B.1: (a) 20 $\times$ 20 μm choroid height images taken from dry tissue by contact mode AFM while image (b) taken from hydrated tissue by tapping mode.

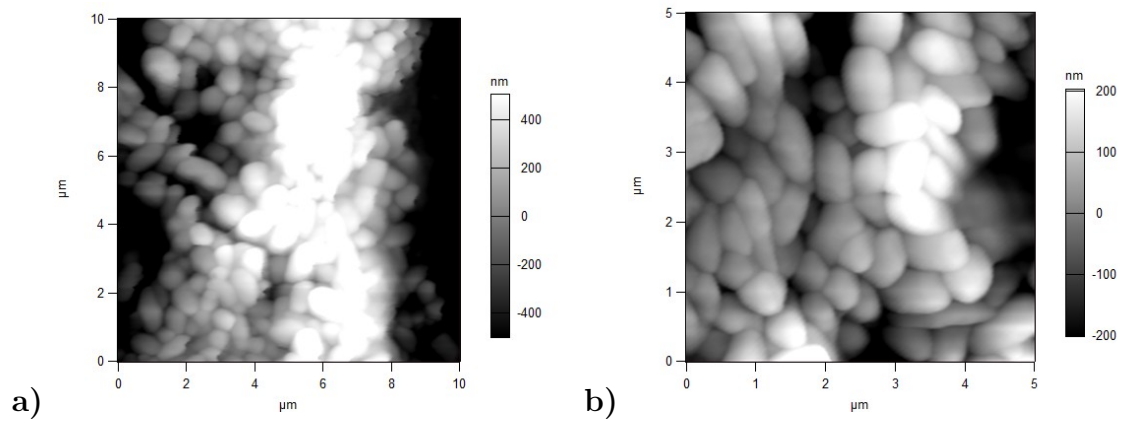

Figure B.2: Zoom 10 × 10 μm (left) and 5 × 5 μm (right) image of the choriocapillaris of the choroid taken from dry sample through contact mode.

To determine the mechanical properties of the choroid, force mapping was obtained through force spectroscopy measurements. A 32 × 32 pixels force mapping was accomplished on 20 × 20 μm of the choroid. The Average Young's modulus of the choroid in dry and hydrated conditions is exhibited in table B.1. The Hertz model was used to determine the Young's modulus of the hydrated tissue while the JKR model was used to determine the Young's modulus of the dry tissue. The reasons for using two different models for analysing the force maps is that in fluid there is no jump to contact and no tip-sample adhesion force, as is indicated in Chapter 3.

The Young's modulus values of dry and hydrated choroid are shown in table B.1 resulted from force mapping plots in Figure B.3. A Welch test showed that the difference between the Young's moduli obtained from dry and hydrated samples is statistically significant ($P = 9.0043 \times 10^{-32}$). This difference in the Young's modulus values is due to the effect of forming a water bridges, which tend to reduce the Young's modulus value.

Table B.1: Average Young's modulus of dry and hydrated choroid tissue and their stander deviation analyzed by the minimal indentation JKR model (a) and Hertz model (b) respectively.

	Young's modulus (MPa) ± standard deviation (MPa)	statistical difference
Dry tissue	29.28 ± 5.342	Yes
Hydrated tissue	0.546 ± 0.125	

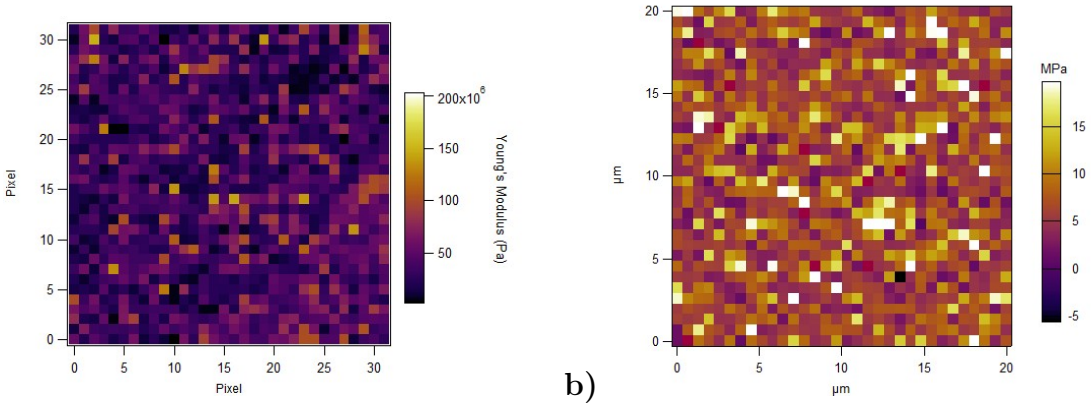

a) b)

Figure B.3: 32 × 32 pixels force maps of the choroid (a) dry tissue and (b) hydrated tissue.

By comparing table 3.5 and B.1, the average Young's modulus of the retina is higher than the average Young's modulus of the choroid. Statistically, the difference between the retina and the choroid was determined, proving that the retina is stiffer than the choroid. The reason behind this difference is not clear yet, but it can be explained based on their structures and functions in the eye. The retina is a very complex tissue and consists of intricately cells, extracellular matrix, blood vessels while the choroid consist mostly of blood vessels and collagen matrix. Besides that, the retina is located at the centre of the eye and exposed to daily stress, which proves the stiffening of the retina.

B.4 Conclusion

As the choroid is associated with many retinal diseases, it is important to map its mechanical properties. Therefore, the morphology and the Young's modulus of the choroid were mapped. Also, we study the effect of hydration on the tissue, which showed statistically significant difference between dry and hydrated tissue. We also demonstrate that the choroid is considerably softer than the retina. This finding can be explained by the different in their structures and functions in the eye.

Appendix C

Sample Statistical Test Output

Below I provide a sample data set and sample output from statistical analyses. One can perform either a Welch test or a single-factor ANOVA test when comparing just two data sets, but the output from both statistical measures are provided here as an example.

C.1 Young's moduli for dry and hydrated samples of retina

Table C.1: Young's moduli of dry and hydrated retina samples

	Young's modulus of dry sample (Pa)	Young's modulus of hydrated sample (Pa)
1	1.06×10^{08}	9.42×10^{05}
2	8.93×10^{07}	9.10×10^{05}
3	7.60×10^{07}	8.73×10^{05}
4	9.47×10^{07}	8.66×10^{05}
5	9.26×10^{07}	7.93×10^{05}
6	9.15×10^{07}	7.34×10^{05}
7	1.10×10^{08}	8.45×10^{05}
8	1.01×10^{08}	8.69×10^{05}
9	7.10×10^{07}	9.32×10^{05}
10	8.45×10^{07}	8.30×10^{05}
11	7.70×10^{07}	8.04×10^{05}
12	8.36×10^{07}	7.90×10^{05}
13	8.00×10^{07}	7.77×10^{05}
14	8.88×10^{07}	8.60×10^{05}
15	9.14×10^{07}	8.78×10^{05}
16	7.00×10^{07}	7.44×10^{05}
17	6.94×10^{07}	5.90×10^{05}
18	7.30×10^{07}	6.32×10^{05}
19	6.80×10^{07}	6.44×10^{05}
20	6.64×10^{07}	5.82×10^{05}
21	6.91×10^{07}	6.01×10^{05}
22	7.02×10^{07}	6.78×10^{05}
23	6.50×10^{07}	6.24×10^{05}
24	6.98×10^{07}	5.94×10^{05}
25	7.05×10^{07}	5.77×10^{05}
26	7.24×10^{07}	6.33×10^{05}
27	7.93×10^{07}	6.74×10^{05}
28	7.35×10^{07}	6.66×10^{05}
29	7.50×10^{07}	6.90×10^{05}
30	7.79×10^{07}	7.01×10^{05}
31	8.07×10^{07}	7.32×10^{05}
32	7.83×10^{07}	7.40×10^{05}

C.2 ANOVA test for dry and hydrated samples

For statistical significance between populations, F > Fc and P < α, which we set as 0.05 (95% confidence). Therefore the two data sets from Table C.1 are statistically distinct, as seen by the parameters given in Table C.2.

Table C.2: Results from the single factor ANOVA test. DF is degrees of freedom; SS is the sum of squares, MS is the mean square, F is the ratio of variances, Fc is the critical F value for the F-test, and P is the calculated probability.

	DF	SS	MS	F	Fc	P
Groups	1	1.00973×10^{17}	1.00973×10^{17}			
Error	62	4.31426×10^{15}	6.95848×10^{13}			
Total	63	1.05287×10^{17}	1.67122×10^{15}	1451.07	3.99589	0

C.3 Welch test for dry and hydrated samples

The Welch test is similar to the Student's t-test and does not require the compared data sets to be of the same size or have the same variance. As with the single factor ANOVA test described above, statistical significance is shown by Fp > Fpc and P < α. As seen in Table C.3, Fp >> Fpc and P << α (α is 0.05, i.e., 95% confidence), and therefore these two data sets are demonstrably distinct.

Table C.3: Results from the Welch test. N1 and N2 are the degrees of freedom, Fp is the Welch statistic (analogous to the F value in the ANOVA test), Fpc is the critical value for Fp, and P is the calculated probability.

N1	1
N2	31
Fp	45.346
Fpc	4.15962
P	1.54954e-77

Bibliography

[1] G. Binnig, C. F. Quate, and C. Gerber. Atomic force microscope. *Physical review letters*, 56(9):930, 1986.

[2] V. J. Morris, A. R. Kirby, and A. P. Gunning. *Atomic force microscopy for biologists*, volume 57. World Scientific, 1999.

[3] C. M. Clancy and J. D. Simon. Ultrastructural organization of eumelanin from Sepia officinalis measured by atomic force microscopy. *Biochemistry*, 40(44):13353–13360, 2001.

[4] Y. Dufrene. *Life at the nanoscale: atomic force microscopy of live cells*. Pan Stanford Publishing, 2011.

[5] F. Braet, R. de Zanger, C. Seynaeve, M. Baekeland, and E. Wisse. A comparative atomic force microscopy study on living skin fibroblasts and liver endothelial cells. *Journal of electron microscopy*, 50(4):283–290, 2001.

[6] L. Li, S. Chen, S. Oh, and S. Jiang. In situ single-molecule detection of antibody-antigen binding by tapping-mode atomic force microscopy. *Analytical chemistry*, 74(23):6017–6022, 2002.

[7] A. M. Baró and R. G. Reifenberger. *Atomic Force Microscopy in Liquid: Biological Applications*. John Wiley & Sons, 2012.

[8] S. Kasas, G. Longo, and G. Dietler. Mechanical properties of biological specimens explored by atomic force microscopy. *Journal of Physics D: Applied Physics*, 46(13):133001, 2013.

[9] K. C. Morton and L. A. Baker. Atomic force microscopy-based bioanalysis for the study of disease. *Analytical Methods*, 6(14):4932–4955, 2014.

[10] J. M. Wallace. Applications of atomic force microscopy for the assessment of nanoscale morphological and mechanical properties of bone. *Bone*, 50(1):420–427, 2012.

[11] NT-MDT. Calibration of the optical detection system.

[12] R. Jagtap and A. Ambre. Overview literature on atomic force microscopy (AFM): Basics and its important applications for polymer characterization. *Indian Journal of Engineering and Materials Sciences*, 13(4):368, 2006.

[13] N. Jalili and K. Laxminarayana. A review of atomic force microscopy imaging systems: application to molecular metrology and biological sciences. *Mechatronics*, 14(8):907–945, 2004.

[14] S. Strasser, A. Zink, M. Janko, W. M. Heckl, and S. Thalhammer. Structural investigations on native collagen type I fibrils using AFM. *Biochemical and biophysical research communications*, 354(1):27–32, 2007.

[15] R. Garcia and A. San Paulo. Attractive and repulsive tip-sample interaction regimes in tapping-mode atomic force microscopy. *Physical Review B*, 60(7):4961, 1999.

[16] C. Putman, K. O. van der Werf, B. G. de Grooth, N. Van Hulst, and J. Greve. Viscoelasticity of living cells allows high resolution imaging by tapping mode atomic force microscopy. *Biophysical journal*, 67(4):1749, 1994.

[17] Y. F. Dufrêne. Recent progress in the application of atomic force microscopy imaging and force spectroscopy to microbiology. *Current opinion in microbiology*, 6(3):317–323, 2003.

[18] N. de Jonge and F. M. Ross. Electron microscopy of specimens in liquid. *Nature nanotechnology*, 6(11):695–704, 2011.

[19] P. Hansma, J. Cleveland, M. Radmacher, D. Walters, P. Hillner, M. Bezanilla, M. Fritz, D. Vie, H. Hansma, and C. Prater. Tapping mode atomic force microscopy in liquids. *Applied Physics Letters*, 64(13):1738–1740, 1994.

[20] J. Legleiter and T. Kowalewski. Insights into fluid tapping-mode atomic force microscopy provided by numerical simulations. *Applied Physics Letters*, 87(16):163120, 2005.

[21] S. Basak and A. Raman. Dynamics of tapping mode atomic force microscopy in liquids: Theory and experiments. *Applied Physics Letters*, 91(6):064107, 2007.

[22] J. E. Sader. Frequency response of cantilever beams immersed in viscous fluids with applications to the atomic force microscope. *Journal of applied physics*, 84(1):64–76, 1998.

[23] K. Takeyasu. *Atomic Force Microscopy in Nanobiology*. CRC Press, 2014.

[24] S. Garcia-Manyes and F. Sanz. Nanomechanics of lipid bilayers by force spectroscopy with AFM: a perspective. *Biochimica et Biophysica Acta (BBA)-Biomembranes*, 1798(4):741–749, 2010.

[25] U. Hartmann. van der Waals interactions between sharp probes and flat sample surfaces. *Physical Review B*, 43(3):2404, 1991.

[26] J. H. Hoh, J. P. Cleveland, C. B. Prater, J. P. Revel, and P. K. Hansma. Quantized adhesion detected with the atomic force microscope. *Journal of the American Chemical Society*, 114(12):4917–4918, 1992.

[27] M. Radmacher, J. P. Cleveland, M. Fritz, H. G. Hansma, and P. K. Hansma. Mapping interaction forces with the atomic force microscope. *Biophysical journal*, 66(6):2159, 1994.

[28] W. F. Heinz and J. H. Hoh. Spatially resolved force spectroscopy of biological surfaces using the atomic force microscope. *Trends in biotechnology*, 17(4):143–150, 1999.

[29] X. Liang, G. Mao, and K. S. Ng. Probing small unilamellar EggPC vesicles on mica surface by atomic force microscopy. *Colloids and Surfaces B: Biointerfaces*, 34(1):41–51, 2004.

[30] A. Vinckier and G. Semenza. Measuring elasticity of biological materials by atomic force microscopy. *Febs Letters*, 430(1):12–16, 1998.

[31] W. C. Young and R. G. Budynas. *Roark's formulas for stress and strain*, volume 7. McGraw-Hill New York, 2002.

[32] C. Rotsch and M. Radmacher. Drug-induced changes of cytoskeletal structure and mechanics in fibroblasts: an atomic force microscopy study. *Biophysical journal*, 78(1):520–535, 2000.

[33] K. S. Worthington, L. A. Wiley, A. M. Bartlett, E. M. Stone, R. F. Mullins, A. K. Salem, C. A. Guymon, and B. A. Tucker. Mechanical properties of murine

and porcine ocular tissues in compression. *Experimental eye research*, 121:194–199, 2014.

[34] M. Boukallel, M. Girot, and S. Régnier. Characterization of cellular mechanical behavior at the microscale level by a hybrid force sensing device. *Journal of the mechanical behavior of biomedical materials*, 2(3):297–304, 2009.

[35] K. L. Johnson, K. Kendall, and A. D. Roberts. Surface energy and the contact of elastic solids. *Proceedings of the Royal Society of London A: Mathematical, Physical and Engineering Sciences*, 324(1558):301–313, 1971.

[36] F. Jin, X. Guo, and H. Gao. Adhesive contact on power-law graded elastic solids: The JKR–DMT transition using a double-Hertz model. *Journal of the Mechanics and Physics of Solids*, 61(12):2473–2492, 2013.

[37] C. Xu. *Nanostructure and Nanomechanics of Collagen Self-Assemblies*. PhD thesis, Memorial University of Newfoundland, 2014.

[38] X. Shi and Y.-P. Zhao. Comparison of various adhesion contact theories and the influence of dimensionless load parameter. *Journal of Adhesion Science and Technology*, 18(1):55–68, 2004.

[39] D. Grierson, E. Flater, and R. Carpick. Accounting for the JKR–DMT transition in adhesion and friction measurements with atomic force microscopy. *Journal of adhesion science and technology*, 19(3-5):291–311, 2005.

[40] J. Chen. Understanding the nanoindentation mechanisms of a microsphere for biomedical applications. *Journal of Physics D: Applied Physics*, 46(49):495303, 2013.

[41] J. Zhang, S. Ebbens, X. Chen, Z. Jin, S. Luk, C. Madden, N. Patel, and C. J. Roberts. Determination of the surface free energy of crystalline and amorphous lactose by atomic force microscopy adhesion measurement. *Pharmaceutical research*, 23(2):401–407, 2006.

[42] Y. F. Dufrêne. Atomic force microscopy of fungal cell walls: an update. *Yeast*, 27(8):465–471, 2010.

[43] M. Baclayon, G. Wuite, and W. Roos. Imaging and manipulation of single viruses by atomic force microscopy. *Soft Matter*, 6(21):5273–5285, 2010.

[44] I. C. Campbell, B. Coudrillier, and C. R. Ethier. Biomechanics of the posterior eye: A critical role in health and disease. *Journal of biomechanical engineering*, 136(2):021005, 2014.

[45] N. R. Galloway, W. M. Amoaku, P. H. Galloway, and A. C. Browning. *Common eye diseases and their management*. Springer Science & Business Media, 2006.

[46] K. Chen, A. P. Rowley, and J. D. Weiland. Elastic properties of porcine ocular posterior soft tissues. *Journal of Biomedical Materials Research Part A*, 93(2):634–645, 2010.

[47] K. Franze, M. Francke, K. Günter, A. F. Christ, N. Körber, A. Reichenbach, and J. Guck. Spatial mapping of the mechanical properties of the living retina using scanning force microscopy. *Soft Matter*, 7(7):3147–3154, 2011.

[48] W. W. Morgan. *Retinal transmitters and modulators: models for the brain*, volume 2. CRC PressI Llc, 1985.

[49] P. Brodal. *The central nervous system: structure and function*. Oxford University Press, 2004.

[50] C. W. Oyster. *The human eye: structure and function*. Sinauer Associates, 1999.

[51] Z.-B. Jin, S. Okamoto, P. Xiang, and M. Takahashi. Integration-free induced pluripotent stem cells derived from retinitis pigmentosa patient for disease modeling. *Stem cells translational medicine*, 1(6):503–509, 2012.

[52] P. L. Kaufman, L. A. Levin, F. H. Adler, and A. Alm. *Adler's Physiology of the Eye*. Elsevier Health Sciences, 2011.

[53] A.-J. F. Carr, M. J. Smart, C. M. Ramsden, M. B. Powner, L. da Cruz, and P. J. Coffey. Development of human embryonic stem cell therapies for age-related macular degeneration. *Trends in neurosciences*, 36(7):385–395, 2013.

[54] J. Sparrrow, D. Hicks, and C. Hamel. The retinal pigment epithelium in health and disease. *Current molecular medicine*, 10(9):802, 2010.

[55] S. P. Daiger, S. J. Bowne, and L. S. Sullivan. Perspective on genes and mutations causing retinitis pigmentosa. *Archives of ophthalmology*, 125(2):151–158, 2007.

[56] T. P. Dryja, T. L. McGee, E. Reichel, L. B. Hahn, G. S. Cowley, D. W. Yandell, M. A. Sandberg, and E. L. Berson. A point mutation of the rhodopsin gene in one form of retinitis pigmentosa. *Nature*, 343(6256):364–366, 1990.

[57] D. T. Hartong, E. L. Berson, and T. P. Dryja. Retinitis pigmentosa. *The Lancet*, 368(9549):1795–1809, 2006.

[58] R. J. Klein, C. Zeiss, E. Y. Chew, J.-Y. Tsai, R. S. Sackler, C. Haynes, A. K. Henning, J. P. SanGiovanni, S. M. Mane, and S. T. Mayne. Complement factor H polymorphism in age-related macular degeneration. *Science*, 308(5720):385–389, 2005.

[59] M. M. Moschos, E. Nitoda, I. P. Chatziralli, and C. A. Demopoulos. Age-Related Macular Degeneration: Pathogenesis, Genetic Background, and the Role of Nutritional Supplements. *Journal of Chemistry*, 2014, 2014.

[60] R. D. Jager, W. F. Mieler, and J. W. Miller. Age-related macular degeneration. *New England Journal of Medicine*, 358(24):2606–2617, 2008.

[61] L. S. Lim, P. Mitchell, J. M. Seddon, F. G. Holz, and T. Y. Wong. Age-related macular degeneration. *The Lancet*, 379(9827):1728–1738, 2012.

[62] J. Ambati and B. J. Fowler. Mechanisms of age-related macular degeneration. *Neuron*, 75(1):26–39, 2012.

[63] M. Killingsworth. Age-related components of Bruch's membrane in the human eye. *Graefe's archive for clinical and experimental ophthalmology*, 225(6):406–412, 1987.

[64] S. B. Mallick and A. Ivanisevic. Study of the morphological and adhesion properties of collagen fibers in the Bruch's membrane. *The Journal of Physical Chemistry B*, 109(41):19052–19055, 2005.

[65] J. Candiello, M. Balasubramani, E. M. Schreiber, G. J. Cole, U. Mayer, W. Halfter, and H. Lin. Biomechanical properties of native basement membranes. *Febs Journal*, 274(11):2897–2908, 2007.

[66] S. B. Mallick, S. Bhagwandin, and A. Ivanisevic. Characterization of collagen fibers in Bruch's membrane using chemical force microscopy. *Analytical and bioanalytical chemistry*, 386(3):652–657, 2006.

[67] J. A. Last, T. Pan, Y. Ding, C. M. Reilly, K. Keller, T. S. Acott, M. P. Fautsch, C. J. Murphy, and P. Russell. Elastic modulus determination of normal and

glaucomatous human trabecular meshwork. *Investigative ophthalmology & visual science*, 52(5):2147, 2011.

[68] C. A. Smith and B. C. Chauhan. Imaging retinal ganglion cells: Enabling experimental technology for clinical application. *Progress in retinal and eye research*, 44:1–14, 2015.

[69] M. R. Hee, C. A. Puliafito, J. S. Duker, E. Reichel, J. G. Coker, J. R. Wilkins, J. S. Schuman, E. A. Swanson, and J. G. Fujimoto. Topography of diabetic macular edema with optical coherence tomography. *Ophthalmology*, 105(2):360–370, 1998.

[70] J. A. IZATT, M. R. HEE, E. A. SWANSON, C. P. LIN, D. HUANG, J. S. SCHUMAN, C. A. PULIAFITO, and J. G. FUJIMOTO. Micrometer-Scale Resolution Imaging of the Anterior Eye In Vivo With Optical Coherence Tomography. *SPIE milestone series*, 165:372–377, 2001.

[71] M. Wojtkowski, V. Srinivasan, J. G. Fujimoto, T. Ko, J. S. Schuman, A. Kowalczyk, and J. S. Duker. Three-dimensional retinal imaging with high-speed ultrahigh-resolution optical coherence tomography. *Ophthalmology*, 112(10):1734–1746, 2005.

[72] G. Scarcelli, R. Pineda, and S. H. Yun. Brillouin optical microscopy for corneal biomechanics. *Investigative ophthalmology & visual science*, 53(1):185, 2012.

[73] D. J. Taatjes, A. S. Quinn, J. H. Rand, and B. P. Jena. Atomic force microscopy: high resolution dynamic imaging of cellular and molecular structure in health and disease. *Journal of cellular physiology*, 228(10):1949–1955, 2013.

[74] D. Xia, S. Zhang, J. Ø. Hjortdal, Q. Li, K. Thomsen, J. Chevallier, F. Besenbacher, and M. Dong. Hydrated human corneal stroma revealed by quantita-

tive dynamic atomic force microscopy at nanoscale. *ACS nano*, 8(7):6873–6882, 2014.

[75] T. Shibata-Seki, K. Tajima, H. Takahashi, H. Seki, J. Masai, H. Goto, E. Kobatake, T. Akaike, and N. Itoh. AFM characterization of chemically treated corneal cells. *Analytical and bioanalytical chemistry*, 407(9):2631–2635, 2015.

[76] Ş. Ţălu, S. Stach, V. Sueiras, and N. M. Ziebarth. Fractal Analysis of AFM Images of the Surface of Bowman's Membrane of the Human Cornea. *Annals of biomedical engineering*, 43(4):906–916, 2015.

[77] M. Lombardo, G. Lombardo, G. Carbone, M. P. De Santo, R. Barberi, and S. Serrao. Biomechanics of the anterior human corneal tissue investigated with atomic force microscopy. *Investigative ophthalmology & visual science*, 53(2):1050–1057, 2012.

[78] J. A. Last, S. M. Thomasy, C. R. Croasdale, P. Russell, and C. J. Murphy. Compliance profile of the human cornea as measured by atomic force microscopy. *Micron*, 43(12):1293–1298, 2012.

[79] C. Labate, M. Lombardo, M. P. De Santo, J. Dias, N. M. Ziebarth, and G. Lombardo. Multiscale Investigation of the Depth-Dependent Mechanical Anisotropy of the Human Corneal StromaMultiscale Stromal Elasticity Probed With AFM. *Investigative ophthalmology & visual science*, 56(6):4053–4060, 2015.

[80] R. L. Gendron, E. Armstrong, H. Paradis, L. Haines, M. Desjardins, C. E. Short, K. A. Clow, and W. R. Driedzic. Osmotic pressure-adaptive responses in the eye tissues of rainbow smelt (Osmerus mordax). *Molecular vision*, 17:2596, 2011.

[81] J. L. Hutter and J. Bechhoefer. Calibration of atomic-force microscope tips. *Review of Scientific Instruments*, 64(7):1868–1873, 1993.

[82] L. Stewart. Determining the Mechanical Properties of Rainbow Smelt (*Osmerus mordax*) Eye Tissue Using Atomic Force Microscopy (AFM). Master's thesis, Memorial University of Newfoundland, 2016.

[83] Y.-B. Lu, K. Franze, G. Seifert, C. Steinhäuser, F. Kirchhoff, H. Wolburg, J. Guck, P. Janmey, E.-Q. Wei, and J. Käs. Viscoelastic properties of individual glial cells and neurons in the CNS. *Proceedings of the National Academy of Sciences*, 103(47):17759–17764, 2006.

[84] G. McDougall. *Nanomechanical Characterization of Murine Vasculature by Atomic Force Microscopy.* Honours thesis, Memorial University of Newfoundland, 2016.

[85] R. L. Gendron, N. V. Laver, W. V. Good, H. E. Grossniklaus, E. Miskiewicz, M. A. Whelan, J. Walker, and H. Paradis. Loss of Tubedown Expression as a contributing factor in the Development of Age-Related Retinopathy. *Invest Ophthalmol Vis Sci*, 51:5267–77, 2010.

[86] J. A. Last, S. J. Liliensiek, P. F. Nealey, and C. J. Murphy. Determining the mechanical properties of human corneal basement membranes with atomic force microscopy. *Journal of structural biology*, 167(1):19–24, 2009.

[87] P. B. Henrich, C. A. Monnier, W. Halfter, C. Haritoglou, R. W. Strauss, R. Y. Lim, and M. Loparic. Nanoscale Topographic and Biomechanical Studies of the Human Internal Limiting MembraneNanoscale Studies of the Human ILM. *Investigative ophthalmology & visual science*, 53(6):2561–2570, 2012.

[88] M. Stacey, D. Dutta, W. Cao, A. Asmar, H. Elsayed-Ali, R. Kelly, and A. Beskok. Atomic force microscopy characterization of collagen 'nanostraws' in human costal cartilage. *Micron*, 44:483–487, 2013.

[89] J. A. van der Rijt, K. O. van der Werf, M. L. Bennink, P. J. Dijkstra, and J. Feijen. Micromechanical testing of individual collagen fibrils. *Macromolecular bioscience*, 6(9):697–702, 2006.

[90] L. Yang, K. O. Van der Werf, C. F. Fitié, M. L. Bennink, P. J. Dijkstra, and J. Feijen. Mechanical properties of native and cross-linked type I collagen fibrils. *Biophysical journal*, 94(6):2204–2211, 2008.

[91] C. A. Grant, D. J. Brockwell, S. E. Radford, and N. H. Thomson. Tuning the elastic modulus of hydrated collagen fibrils. *Biophysical journal*, 97(11):2985–2992, 2009.

[92] C. A. Grant, D. J. Brockwell, S. E. Radford, and N. H. Thomson. Effects of hydration on the mechanical response of individual collagen fibrils. *Applied Physics Letters*, 92(23):233902, 2008.

[93] E. Yamamoto, T. Akimoto, M. Yasui, and K. Yasuoka. Origin of subdiffusion of water molecules on cell membrane surfaces. *Scientific reports*, 4, 2014.

[94] G. Moeller. AFM nanoindentation of viscoelastic materials with large end-radius probes. *Journal of Polymer Science Part B: Polymer Physics*, 47(16):1573–1587, 2009.

[95] Z. Wu, T. A. Baker, T. C. Ovaert, and G. L. Niebur. The effect of holding time on nanoindentation measurements of creep in bone. *Journal of biomechanics*, 44(6):1066–1072, 2011.

[96] D. R. Baselt and J. D. Baldeschwieler. Imaging spectroscopy with the atomic force microscope. *Journal of applied physics*, 76(1):33–38, 1994.

[97] E. M. Darling. Force scanning: a rapid, high-resolution approach for spatial mechanical property mapping. *Nanotechnology*, 22(17):175707, 2011.

[98] R. F. Spaide, K. Ohno-Matsui, and L. A. Yannuzzi. *Pathologic myopia*. Springer, 2014.

[99] J. Kur, E. A. Newman, and T. Chan-Ling. Cellular and physiological mechanisms underlying blood flow regulation in the retina and choroid in health and disease. *Progress in retinal and eye research*, 31(5):377–406, 2012.

[100] S. Sonoda, T. Sakamoto, T. Yamashita, M. Shirasawa, E. Uchino, H. Terasaki, and M. Tomita. Choroidal structure in normal eyes and after photodynamic therapy determined by binarization of optical coherence tomographic images. *Investigative ophthalmology & visual science*, 55(6):3893–3899, 2014.